Daniel Obiora Iruikwu

In Plane Numerical Analysis of Mechanical Stress in a Synchronous Reluctance Machine

School of Electrical Engineering

Thesis submitted for examination for the degree of Master of Science in Technology.

Espoo 12.08.2013

Thesis supervisor:

Prof. Antero Arkkio

Thesis advisors:

Prof. Anouar Belahcen

M.Sc. Deepak Singh

Aalto University
School of Electrical Engineering

AALTO UNIVERSITY
SCHOOL OF ELECTRICAL ENGINEERING

ABSTRACT OF THE
MASTER'S THESIS

Author: Daniel Obiora Iruikwu

Title: In Plane Numerical Analysis of Mechanical Stress in a Synchronous Reluctance Machine

Date: 12.08.2013 Language: English Number of pages:7+65

Department of Electrical Engineering

Professorship: Electromechanics Code: S-17

Supervisor: Prof. Antero Arkkio

Advisors: Prof. Anouar Belahcen, M.Sc. Deepak Singh

The distortion due to the mechanical stresses from manufacturing issues and the operation of electrical machines are known to have adverse effect on the magnetic properties of electrical iron core and due to the stress dependency of iron core losses, it is therefore imperative that we account for the stresses from the different conditions causing mechanical stresses in a rotating electrical machine.

This work presents a 2-D FE-analysis of the mechanical stresses due to shrink fitting, centrifugal forces and the magnetic forces in a 4-pole, 3-phase synchronous reluctance machine at rated frequency of 50 Hz. The stresses due to shrink fitting and centrifugal forces were computed by solid mechanics method, while the stresses due to magnetic forces were computed using both magnetic field method and solid mechanics method. The total mechanical stress distributions from all stress sources were obtained using a weakly coupled approach. It was found that shrink fitting causes a very large tensile stress at the rotor core and compressive stress in most part of the stator yoke, but have almost no effect at the stator teeth. The centrifugal forces also contribute to the total tensile stress of the rotor core. The magnetic forces have the least effect on the total stress distribution of the machine.

The combined stresses obtained are mostly tensile at the rotor core and compressive at most part of the stator yoke, while the stator teeth were under low tensile stress due to the magnetic forces. The presence of flux barriers between flux paths at the rotor core causes large stresses to distribute at the bridge between flux barriers near the fit interface. Increase or decrease of the radial interference and/or frequency increases or reduces the total mechanical stress distribution of the machine.

Keywords: mechanical stress, shrink fitting, centrifugal force, magnetic forces, solid mechanics, rotating machinery method, FE-analysis, weakly coupled

Preface

This master's thesis has been supervised by the electromechanical group at the department of electrical engineering of Aalto University, Finland and was funded from the FCEP project by TEKES. I wish to extend my heart felt gratitude to everyone who has played important roles all through my journey in the course of this thesis writing.

Firstly, I want to extend my sincere gratitude to my supervisor, Prof. Antero Arkkio for given me the opportunity to be part of this group. As a member of the research group and a student of the department, you have enlightened me. I also want to thank my advisor, Prof. Anouar Belahcen for his guidance which has kept me in the right path through the course of this project; I will not forget the time spend in checking my work.

Secondly, my sincere thanks go to Deepak Singh for his advice and support during this work. My thanks also goes to Paavo Rasilo and Javiar Martinez for their advice and support, Mr. Ari Havisto for his help in making my work technically easier by providing the necessary technical tools needed for this project. I also want to thank my colleague and friends, Jonathan S.Velasco and Sahas S. Bikram whose presence have created an environment filled with humour and friendship and to all members of the electromechanical group, I say thank you for your support.

Finally, I want to thank my parents, Mr. Onosike Iruikwu and Mrs. Georgina Irukwu for their moral and spiritual support, my brother and friend Kingsley Irukwu for his advice that has pulled me up in times of discouragement and most importantly I want to thank God almighty for the life, health and the wisdom that I have been flourished with. "It is of the Lord's mercies that we are not consumed, because his compassions fail not. Lam 3:22".

Otaniemi, 12.08.2013 Daniel O. Iruikwu

Contents

List of symbols and abbreviations

Symbols

$\boldsymbol{A}$	magnetic vector potential
A	z-component of $\boldsymbol{A}$
A	lamé's coefficient
a, b, c	dimensions of cylindrical geometry
$\boldsymbol{B}$	magnetic flux density
$\hat{B}$	peak flux density
B	lamé's coefficient
C	4th order elasticity tensor
$\mathrm{C_{i,j}}$	arbitrary constants
$\boldsymbol{D}$	electric flux density
d	lamination thickness or out-of-plane thickness
$\boldsymbol{E}$	electric field strength
E	Young's modulus
E_i	Young's modulus of inner cylinder
E_o	Young's modulus of outer cylinder
$\boldsymbol{e}_\mathrm{z}$	unit vector parallel to the z-axis
$\boldsymbol{F}$	force
F_c	centrifugal force of rotating shaft and rotor
$\boldsymbol{F}_V$	volume force density
f	frequency
$\boldsymbol{H}$	magnetic field strength
I	current
$\boldsymbol{J}$	current density
J	z-component of $\boldsymbol{J}$
$\mathrm{k_e}$	coefficient of eddy-current losses
$\mathrm{k_h}$	coefficient of hysteresis losses
l	length of the conductor
P_e	eddy-current losses
P_{ex}	excess losses
P_{Fe}	total iron losses
P_h	hysteresis losses
p_c	contact pressure
R	resistance
r, φ, z	coordinates of a cylindrical coordinate system
S	cross-sectional area
s_0	initial stress
T	current temperature
T_ref	reference temperature
t	time
$\boldsymbol{u}$	scalar potential difference

u	displacement
u_i	interface displacement at inner cylinder
u_o	interface displacement at outer cylinder
x, y, z	Cartesian components

Greek symbols

α	thermal expansion tensor
γ	Steinmetz coefficient
δ	radial interference or interference displacement
ϵ	strain
ϵ_0	initial strain
ϵ_r	radial strain
$\epsilon_\mathrm{x,y,z}$	principal strain in direction x,y or z
ϵ_θ	tangential strain
μ	permeability of material
μ_0	permeability of a vacuum
μ_r	relative permeability
ν	reluctivity
ρ	mass density
ρ_i	mass density of inner cylinder
ρ_o	mass density of outer cylinder
σ	mechanical stress
σ_r	radial stress
σ_ri	radial stress at inner cylinder
σ_ro	radial stress at outer cylinder
$\sigma_\mathrm{x,y,z}$	principal stress in direction x,y or z
σ_θ	hoop, circumferential or tangential stress
$\bar{\sigma}$	conductivity
υ	Poisson ratio
υ_i	Poisson ratio of inner cylinder
υ_o	Poisson ratio of outer cylinder
Φ	electric scalar potential
Ω	integration surface
ω	rotational speed or angular velocity

Abbreviations

2-D	two-dimensions
FE	finite element
FEM	finite-element-method
FPS	first principal stress
SynRM	synchronous reluctance motor

1 Introduction

1.1 Background

An electrical machine is a device which converts electrical energy to mechanical energy and vice versa. In rotating electrical machines, the energy conversion process involves the use of magnetic materials which amplify and direct the magnetic flux that act on the medium thereby producing torque and machine output.

In the past decades, several developments have been made in the optimization and improvement of rotating electrical machine design and this trend has led to the development of models that evaluate losses in electrical machines with the opt for developing efficient model which enables the design of machine with minimum losses. Several researches have been made and models have been developed which account for the various contribution of losses in electrical machines. The computation of the iron core losses is imperative in the evaluation of machine efficiency. Accounts from recent research have shown that iron core losses are stress dependent and that mechanical stresses have adverse effect on the magnetic properties of electrical iron lamination sheet. The mechanical stresses in the iron core of a rotating electrical machine can be caused by different manufacturing processes such as shrink fit or force fit of the shaft to rotor core and the stator to the machine frame, cutting or punching of the stator slots and the rotor slots in the case of induction machines, stamping and other conditions such as centrifugal forces on the rotating rotor and magnetic forces caused by the rotating magnetic field.

In this work, the 2-D finite-element analysis of the mechanical stresses due to shrink fitting, centrifugal forces and magnetic forces in the rotor and stator core of a synchronous reluctance machine are investigated. The knowledge of these stresses is important in the analysis of iron core losses. Iron loss is important issue in synchronous reluctance machine as it could result to the main source of power loss. The problem of core losses has been an important subject in the design of electrical machine and has led to several experimental investigations in attempt to develop an efficient model for the computation of total iron core losses.

The magnetic properties of electrical machine are known to be affected by mechanical stresses. These stresses could result from manufacturing issues such as shrink fitting, stamping, punching and cutting, or from centrifugal forces and magnetic forces in a rotating electrical machine. The analysis of the total iron core losses is important in the design optimization of electrical machines and because of the stress dependency of iron core losses; the knowledge of the mechanical stress distribution in the electrical machine is important.

The subject of magneto-mechanical effect on ferromagnetic material is also important subject which gives the purpose of this thesis a meaning. The subject describes the change in the magnetization of magnetic materials resulting from a change in

applied stress under a constant applied field. In the past decades, several experimental investigations have been made to demonstrate the stress dependency on magnetization in ferromagnetic materials and also in the stress effect in iron core losses. An overview of some of the researches on this subject shall be discuss in the next section of this thesis.

1.2 Objective of this Work

The objective of this work is to develop a 2-D finite-element analysis of the mechanical stress distribution in a synchronous reluctance machine. The stresses should account for the effect of shrink fitting from manufacturing process, the centrifugal forces from the rotating shaft and rotor core and magnetic forces from the rotating magnetic field. Furthermore, the total mechanical stresses distribution due to shrink fitting and magnetic forces at the stator core and that due to shrink fitting, centrifugal force and magnetic forces at the rotor core and shaft are computed for the synchronous reluctant machine.

1.3 Thesis Outline

Finite–element method (FEM) is an important tool in the field of engineering and it plays an important role in predicting the characteristics of engineering materials. In this work, finite-element-method is used in the numerical computation of the mechanical stress distribution and also predicting the stress distribution in a reluctance machine model.

In this Section, we have introduced the purpose and objectives of this thesis and the background of this work has been briefly discussed. Section 2 is the literature review of some scientific work which plays important roles to the purposes and objectives of this thesis. Section 3 will present a detailed description of the methods implemented in this work while the results obtained from the investigation are presented in Section 4 with detailed interpretation of the findings. Finally, the results of the investigation are discussed in Section 5 with statement of challenges encountered and how to remedy these challenges for future investigation.

2 Literature Review

The aim of this work is to predict the two-dimensional mechanical stress distribution in a synchronous reluctance machine due shrink-fit, centrifugal forces and magnetic forces by finite-element method. The knowledge of the stresses and the conditions that cause the stress distributions are important in the computation of iron loss in electrical iron sheet; owing to the stress dependency of iron loss. This knowledge is also useful in the design optimization of electrical machines, such that the stress dependent factors conditions (such as radial interference in shrink fitting) are implemented in design optimization to obtain a machine with minimal stress and core losses.

In this section, researches which give important insights to the objective of this thesis are discussed. This includes the magnetic and mechanical analysis, forces, shrink fit, stress computation, iron losses and stress, magnetization curve and stress and coupled magneto-mechanical analysis.

2.1 Magnetic Field Analysis

In the study of electrical machines, knowledge of the magnetic field is needed in the machine design. The magnetic field may be solved from the Maxwell equations. However, the solutions of field equations are laborious due to the complicated geometries and the nonlinearity due to the saturation of iron core. The magnetic field is computed using finite element method in two-dimensions. In this work, the finite element method used is based on the $\boldsymbol{A}$–Φ formulation of the magnetic field.

Maxwell's Equations

$$\nabla \times \boldsymbol{E} = -\frac{\partial \boldsymbol{B}}{\partial t} \tag{2.1}$$

$$\nabla \times \boldsymbol{H} = \boldsymbol{J} + \frac{\partial \boldsymbol{D}}{\partial t} \tag{2.2}$$

$$\nabla \cdot \boldsymbol{D} = \rho \tag{2.3}$$

$$\nabla \cdot \boldsymbol{B} = 0 \tag{2.4}$$

In the work by (Arkkio, 1987), an electrical machine is treated as a quasi-static magnetic system and the Maxwell's equations are reduced to

$$\nabla \times \boldsymbol{E} = -\frac{\partial \boldsymbol{B}}{\partial t} \tag{2.5}$$

$$\nabla \times \boldsymbol{H} = \boldsymbol{J} \tag{2.6}$$

and the constitutive material relations are

$$\boldsymbol{H} = \nu \boldsymbol{B} \tag{2.7}$$
$$\boldsymbol{J} = \bar{\sigma} \boldsymbol{E} \tag{2.8}$$

Using the magnetic vector potential $\boldsymbol{A}$ and electric scalar potential Φ given by

$$\boldsymbol{B} = \nabla \times \boldsymbol{A} \tag{2.9}$$
$$\boldsymbol{E} = -\frac{\partial \boldsymbol{A}}{\partial t} - \nabla \Phi \tag{2.10}$$

The equations for the vector and scalar potential obtained are by substitution, these are given as

$$\nabla \times \left(\nu \nabla \times \boldsymbol{A}\right) + \bar{\sigma} \frac{\partial \boldsymbol{A}}{\partial t} + \bar{\sigma} \nabla \Phi = 0 \tag{2.11}$$
$$\nabla \cdot \left(\bar{\sigma} \frac{\partial \boldsymbol{A}}{\partial t}\right) + \nabla \cdot \left(\bar{\sigma} \nabla \Phi\right) = 0 \tag{2.12}$$

The "Coulomb's gauge" condition is commonly used for the sake of solution uniqueness. This condition is satisfied implicitly in two-dimensional cases and is given by

$$\nabla \cdot \boldsymbol{A} = 0 \tag{2.13}$$

The possibility of a two-dimensional model, in which the geometry and material properties are independent of the z-coordinate, makes the solution of field equation much easier to obtain. The vector potential and current density are given by

$$\begin{aligned} \boldsymbol{A} &= A(x, y, t) \boldsymbol{e}_{\mathrm{z}} \\ \boldsymbol{J} &= J(x, y, t) \boldsymbol{e}_{\mathrm{z}} \end{aligned} \tag{2.14}$$

Where x and y are Cartesian spatial coordinates and $\boldsymbol{e}_{\mathrm{z}}$ is a unit vector parallel to the z-axis. The components of the flux density in two-dimensional field problems in the Cartesian coordinate system are

$$B_x = \frac{\partial A}{\partial y} \tag{2.15}$$
$$B_y = -\frac{\partial A}{\partial x} \tag{2.16}$$

The two-dimensional formulation for a voltage driven electrical machine connected to the network with conductor of cross-section S has the voltage equation

$$\boldsymbol{u} = RI + R \int_S \bar{\sigma} \frac{\partial \boldsymbol{A}}{\partial t} \cdot \mathrm{d}\mathbf{S} \tag{2.17}$$

This is solved simultaneously with equations (2.11) and (2.12). The complete derivation is given in (Arkkio, 1987). The equation for the vector potential obtained is given by

$$\nabla \times \left(\nu \nabla \times \boldsymbol{A}\right) + \bar{\sigma} \frac{\partial \boldsymbol{A}}{\partial t} = \frac{\bar{\sigma}}{l} \mathrm{U} \boldsymbol{e}_{\mathrm{z}} \tag{2.18}$$

Where U is the potential difference between ends of the conductor, $\bar{\sigma}$ is the conductivity, l is the length of the conductor. The expression (2.18) is implemented in finite-element methods to solve magnetic field problems in electrical machines.

2.1.1 Magnetic Forces Calculation

In this section, overviews of some methods used in the calculation of the magnetic forces are discussed. The magnetic forces acting on a ferromagnetic material in electrical machines are of two kinds: the magnetization forces and the $\boldsymbol{J} \times \boldsymbol{B}$ forces (Kank et al., 2006). There exist several formulation for computing magnetic forces which give the same total force acting on a machine surrounded by air (Carpenter, 1960; Bastos and Sadowski, 2003; Bianchi, 2005). These formulations are either based on the solutions from the vector potential equations or the force density over the magnetic surfaces. The methods used in the computation of magnetic forces include

1. Maxwell stress tensor method
2. Virtual Work Method
3. Lorentz force method

In the computation of magnetic forces, the two methods that are often used today are the Maxwell's stress tensor method and the principle of virtual works method; though there have not been any official agreements as to which formulation best describe the mechanical effect of magnetism.

2.1.1.1 Maxwell Stress Tensor Method

The Maxwell's stress tensor permits the fast computation of the magnetic forces acting on a body in an electromagnetic field. This method is extensively used in computer programs for the numerical computation of magnetic field problems and is applied in the calculation of magnetic forces acting on the rotor or stator of rotating electrical machine.

In this method, the forces are calculated by first selecting the surface that encloses the machine part e.g. rotor or stator of the machine. We then integrate over the enclosed surface; in which the quantities are defined by the potential which describes the domain. For a body characterized by permeability μ_0 and flux density $\boldsymbol{B}$, the Maxwell's stress tensor expressed in the Cartesian coordinate system is given as

$$\boldsymbol{\tau} = \frac{1}{\mu_0}\begin{bmatrix} B_x^2 - \frac{1}{2}\boldsymbol{B}^2 & B_xB_y & B_xB_z \\ B_yB_x & B_y^2 - \frac{1}{2}\boldsymbol{B}^2 & B_yB_z \\ B_zB_x & B_zB_y & B_z^2 - \frac{1}{2}\boldsymbol{B}^2 \end{bmatrix} \tag{2.19}$$

Applying the divergence of the stress tensor gives the force density of the body. The total force of the body is obtained by the volume integral of the force density (Bastos and Sadowski, 2003; Belahcen, 2004). For an enclosed cylindrical surface Γ in an air gap of a machine, the total magnetic force acting on the body reduced to

$$\boldsymbol{F} = \oint_{\Gamma}\left(\frac{1}{\mu_0}B_n\boldsymbol{B} - \frac{1}{2\mu_0}\boldsymbol{B}^2\boldsymbol{n}\right)\mathrm{d}\Gamma \tag{2.20}$$

this is also expressed as

$$\boldsymbol{F} = \oint_{\Gamma}\left(\frac{1}{2\mu_0}(B_n^2 - B_t^2)\boldsymbol{n} + \frac{1}{\mu_0}B_nB_t\boldsymbol{t}\right)\mathrm{d}\Gamma \tag{2.21}$$

where $\boldsymbol{n}$ and $\boldsymbol{t}$ are the normal and tangential unit-vector outward to the differential surface $\mathrm{d}\Gamma$ respectively. This method was implemented in the computation of the forces on a rotor slot region in (Kank et al., 2006). It was found that the forces in these region have two components: one due to the $\boldsymbol{J} \times \boldsymbol{B}$ force acting on the rotor conductor while the other is the magnetization force which acts on the rotor core.

2.1.1.2 Virtual Work Method

This method uses the principle of virtual work for calculating magnetic forces. It is based on the variation of the energy between two different positions and thus

comparing the energy balance between two different position which correspond to the virtual change of the object position in the direction of the force computation (Bianchi, 2005). The Magnetic forces are obtained as a derivative of the energy or co-energy versus the displacement of the moveable parts. For an electrical machine with vector potential $\boldsymbol{A}$, the magnetic energy is given by

$$W = \int_{\Omega} \left(\int_{0}^{\mathrm{B}} \boldsymbol{H} \cdot \mathrm{d}\boldsymbol{B} \right) \mathrm{d}\Omega \tag{2.22}$$

and the total magnetic force acting on the machine is given by

$$\boldsymbol{F} = -\frac{\partial W}{\partial \mathbf{s}} \tag{2.23}$$

The methodology for theoretical and numerical computation of the global magnetic and electric force acting on movable electromagnetic devices are presented in (Coulomb, 1983; Coulomb and Meunier, 1984).

2.1.1.3 Lorentz Force Method

This method is used to calculate the total force acting on a current carrying conductor due to magnetic field. The force density within the conductor is given by $\boldsymbol{J} \times \boldsymbol{B}$. The total force obtained by volume integration is given by

$$\boldsymbol{F} = \int_{V} \Big(\boldsymbol{J} \times \boldsymbol{B} \Big) \mathrm{dV} \tag{2.24}$$

Where $\boldsymbol{J}$ is the current density and $\boldsymbol{B}$ is the magnetic flux density.

The radial component (stress) and the circumferential component (shear) are obtained by separating the quantity inside the integral in equation (2.21). This replaces the indices n and t with r and φ for a cylindrical rotor surface; we have

$$\sigma_{\mathrm{r}} = \frac{1}{2\mu_0} \Big(B_{\mathrm{r}}^2 - B_{\varphi}^2 \Big) \tag{2.25a}$$

$$\sigma_{\theta} = \frac{1}{\mu_0} \Big(B_{\mathrm{r}} B_{\varphi} \Big) \tag{2.25b}$$

2.2 Mechanical Analysis

The knowledge of the stress in a rotating electrical machine is imperative for machine efficiency evaluation; owing to the stress dependency of iron losses. The factors which cause the losses in electrical machines could be attributed to the movement of domain walls in the micro-structures due to mechanical or electrical processes.

The mechanical analysis of electrical machines describes the major transition caused by mechanical processes involving the materials' response to the forces: which could be elastic properties causing mechanical stresses, deformation or loss energy as heat from damping effect in the case of applied oscillatory or pulsing forces (Menard, 2002). The mechanical analyses of an electrical machine simply predict the changes in the displacement field and properties of the iron core material when subjected to an external applied load.

The change in the displacement field causes changes in the machine structural geometry which result to mechanical stresses. These stresses in rotating electrical machines could be due to issues from manufacturing processes such as cutting or punching of the winding slots, stamping and shrink fitting. They could also occur in the operation of the electrical machine; as centrifugal forces at the rotating rotor core and electromagnetic forces from the rotating magnetic field. Predicting the mechanical stress distribution in a synchronous reluctance machine is the goal of this work and in order to achieve this goal, it is important to understand how these stresses are computed. This shall be discussed in the next section.

2.2.1 Stress Calculation

The effect of mechanical stress can be seen in any engineering structure or mechanism which is subjected to an external force arising from the service condition or the environment in which the component operates; for example, an electrical machine is subjected to magnetic forces in a magnetic field. If the components or members are in equilibrium, the resultant external force will be zero, but the reaction (internal forces) set up within the material tend to deform the members. The deformation of the member is the result of the force acting per unit area on the member. Thus

$$\text{Stress } \sigma = F/S \tag{2.26}$$

Where F is the force acting on the cross-sectional area S of the structure. The stress acting on a component can be either tensile (positive) stress or compressive (negative) stress.

Principal stresses

In the case of any stress tensor $\boldsymbol{\tau}$, there is a coordinate system where all off-diagonal components are zero (shear stress vanishes), whereas the diagonal com-

ponents are non-vanishing. The remaining normal stress components are called *principal stresses*. These stress components are

$$\sigma_{\mathrm{x}} = \frac{E}{(1+\upsilon)(1-2\upsilon)}\left[(1-\upsilon)\epsilon_{\mathrm{x}} + \upsilon(\epsilon_{\mathrm{y}} + \epsilon_{\mathrm{z}})\right] \tag{2.27a}$$

$$\sigma_{\mathrm{y}} = \frac{E}{(1+\upsilon)(1-2\upsilon)}\left[(1-\upsilon)\epsilon_{\mathrm{y}} + \upsilon(\epsilon_{\mathrm{z}} + \epsilon_{\mathrm{x}})\right] \tag{2.27b}$$

$$\sigma_{\mathrm{z}} = \frac{E}{(1+\upsilon)(1-2\upsilon)}\left[(1-\upsilon)\epsilon_{\mathrm{z}} + \upsilon(\epsilon_{\mathrm{x}} + \epsilon_{\mathrm{y}})\right] \tag{2.27c}$$

These expressions are generally implemented in finite-element software for calculating the mechanical stresses in a geometry when the shear stresses are neglected.

2.2.2 Shrink Fitting

Shrink fitting is a manufacturing process which involves fitting of one cylinder over another. It is usually done for two or more cylinders; the smaller cylinder with outer diameter slightly larger than the inner diameter of the bigger cylinder as shown in Figure 1. The bigger cylinder is heated until the inner diameter is expanded; subsequently, it is slide onto the smaller cylinder and allowed to cool to room temperature: for which both the smaller (inner) and bigger (outer) cylinders attain a common radius c called the *joint radius*. The initial extra radial length on the outer radius of the inner cylinder before the shrink fitting is known as the *radial interference*.

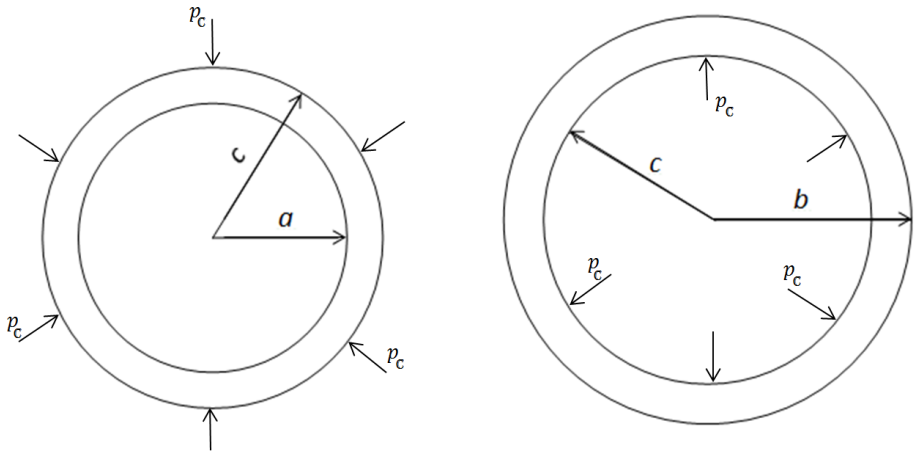

Figure 1: Geometry of inner (left) and outer (right) cylinders after shrink-fit.

The stress distribution due to shrink fitting result can be calculated analytically from a simple expression known as the Lamé's equation. This method neglects the effect of temperature and it is easily applied when the contact pressure p_{c} in the shrink fitted geometry is known and the geometry is cylindrical and symmetric; consequently there is no shearing stress in the transverse plane therefore setting the

principle stresses on that plane (Hearn, 1997*a*,*b*). The radial and tangential stress distribution as stated in (Takahashi and Miyagi, 2011; Hamrock et al., 1999; Özel et al., 2005) for the inner cylinder are given by

$$\sigma_{\mathrm{r}} = \frac{p_c c^2}{c^2 - a^2}\left(\frac{a^2}{c^2} - 1\right) \tag{2.28}$$

$$\sigma_{\theta} = \frac{p_c c^2}{c^2 - a^2}\left(\frac{a^2}{c^2} + 1\right) \tag{2.29}$$

while for the outer cylinder, the stresses are given by

$$\sigma_{\mathrm{r}} = \frac{p_c c^2}{b^2 - c^2}\left(1 - \frac{b^2}{c^2}\right) \tag{2.30}$$

$$\sigma_{\theta} = \frac{p_c c^2}{b^2 - c^2}\left(1 + \frac{b^2}{c^2}\right) \tag{2.31}$$

σ_{r} and σ_{θ} are the radial and circumferential stress respectively and a, b and c are the radii of the compound cylinder. The total radial interference for the shrink-fitted geometry is given by

$$\delta = c p_c\left[\frac{b^2 + c^2}{E_{\mathrm{o}}(b^2 - c^2)} + \frac{\upsilon_{\mathrm{o}}}{E_{\mathrm{o}}} + \frac{c^2 + a^2}{E_{\mathrm{o}}(c^2 - a^2)} - \frac{\upsilon_{\mathrm{i}}}{E_{\mathrm{i}}}\right] \tag{2.32}$$

$E_{\mathrm{i}}, \upsilon_{\mathrm{i}}$ and $E_{\mathrm{o}}, \upsilon_{\mathrm{o}}$ are the Young's Modulus and Poisson ratio of the inner and outer cylinders respectively. These expressions are implemented in the solutions of the analytical problems for shrink-fit computation in cylindrical geometries.

The stress distribution due to shrink-fit in a symmetric isotropic material can also be obtained more accurately using the expression for a plain-strain condition given in (Bickford, 1998). In this expression, the physical material properties are taken into consideration in the stress calculations. Neglecting the effect of change in temperature, the equation for the radial, tangential and axial stresses for a shrink fitted cylindrical geometry are given as

$$\sigma_{\mathrm{r}} = \frac{E}{(1 + \upsilon)(1 - 2\upsilon)}\big((1 - \upsilon)\epsilon_{\mathrm{r}} + \upsilon\epsilon_{\theta}\big) \tag{2.33}$$

$$\sigma_{\theta} = \frac{E}{(1 + \upsilon)(1 - 2\upsilon)}\big((1 - \upsilon)\epsilon_{\theta} + \upsilon\epsilon_{\mathrm{r}}\big) \tag{2.34}$$

$$\sigma_{\mathrm{z}} = \upsilon\big(\sigma_{\mathrm{r}} + \sigma_{\theta}\big) \tag{2.35}$$

ϵ_{r} and ϵ_{θ} are the radial and tangential strain.

Researches that have investigated the effect of shrink fitting on the magnetic properties of iron core in electrical machines are few. Some of the recent investigations on this subject are discussed here.

Fujisaki et al. (2005) demonstrated experimentally the effected of shrink fit and stamping on the mechanical stress and iron loss distribution on the electrical steel of stator core. The investigation was accompanied by a numerical calculation of the iron loss distribution in comparison to the experimental measurements (Fujisaki et al., 2007). Data obtained reveal that iron loss decreases with a decrease in the compressive mechanical stresses resulting from shrink fitting. The results also show that the iron loss become larger as the width of shrink fit increases.

Takahashi et al. (2008) also investigated the effect of compressive stress from shrink fit on magnetic properties of electrical motor core. The analysis examined shrink fit, punching and the effect of eddy current loss on a permanent magnet motor; comparing the finite-element method results with measurement results. The B-H curve and iron loss of stator core of an actual shrink-fit motor were measured. The stress effect of the shrink fitting was found to cause about 50% reduction in permeability, while the iron losses were increased by 30% in comparison to the result obtained without shrink-fit. Furthermore, Takahashi and Miyagi (2011) analyzed the mechanical stress distribution due to shrink fit of motor core and also examined the mechanical stresses in the circumferential and radial directions using strain gauges. The experimental data shows that large compressive stresses develop at the stator yoke due to shrink-fit. The effect of compressive stress in the longitudinal direction of a non-oriented electrical steel lamination grade was also measured. Takahashi found that at compressive mechanical stress less than 50 MPa the permeability decreased and iron loss increased rapidly.

2.3 Iron Losses and Stresses

The prediction of iron loss in electrical iron steel sheet has been a difficult and challenging task in spite of the numerous numbers of researches done in the field of electromagnetics and in electrical machines modeling. This has led to the development of several models for predicting iron losses in electrical steel sheets. In recent years, several researches have been made which studied the stress dependency of iron losses in electrical steel sheets; some of these literatures are reviewed here.

2.3.1 Theory of Iron Losses

The investigation of the losses in ferromagnetic laminations when supplied by a sinusoidal flux waveform was conducted by Steinmetz (1892) and Bertotti (1988). They found that the losses approximately obeys certain power function of the magnetization frequency f and the peak flux density $\hat{\mathrm{B}}$. The total iron loss was separated by Steinmetz into losses from magnetic hysteresis and eddy-currents expressed as

$$\begin{aligned} P_{\mathrm{Fe}} &= P_{\mathrm{h}} + P_{\mathrm{e}} \\ &= \mathrm{k_h} f \hat{B}^{1.6} + \mathrm{k_e} f^2 \hat{B}^2 \end{aligned} \tag{2.36}$$

$\mathrm{k_h}$ and $\mathrm{k_e}$ are coefficient that depend on material properties. Over the years, several different modifications have been made on the so called loss separation approach. Bertotti separated by statistical theory the total iron losses in soft ferromagnetic material into hysteresis loss, classical loss and the excess loss with the frequency and sinusoidal peak flux density expressed as

$$\begin{aligned} P_{\mathrm{Fe}} &= P_{\mathrm{h}} + P_{\mathrm{e}} + P_{\mathrm{ex}} \\ &= \mathrm{k_h} f \hat{B}^{\gamma} + \frac{\bar{\sigma}\pi^2 d^2}{6} f^2 \hat{B}^2 + 8\sqrt{\bar{\sigma}\mathrm{G}S\mathrm{V_0}} f^{1.5} \hat{B}^{1.5} \end{aligned} \tag{2.37}$$

where $\mathrm{V_0}$ is a fitting parameter with dimensions of magnetic field describing microstructural features, d and S are the thickness and cross-sectional area of the lamination respectively, $\bar{\sigma}$ is the conductivity of the lamination material, $\mathrm{G} = 0.1357$ and γ is a Steinmetz coefficient which was found by Foster et al. (1982) in a measurement to study the B^{γ} dependency of $\mathrm{P_h}$ give $\gamma = 2$ for oriented Si steels and 1.6 for other samples which is in agreement with Steinmetz.

In recent times, several authors have adapted the use of the statistical theory in iron loss computation. On the other hand, Graham (1982) emphasized that losses in conducting ferromagnetic materials is the joule heating caused by the flow of eddy-current around moving domain walls and Zhang et al. (2011) developed a dynamic hysteresis finite-element model for core losses calculation for frequencies up to 4000 Hz and thickness up to 0.635 mm based on Steinmetz formula but including

some physical phenomenon absent in Steinmetz formulation.

In view of the accuracy of the convectional loss separation technique, Zirka et al. (2010) evaluation shows that the main reason for inaccuracy in analytical computation is by reason of the use of simplified equation for the classical eddy-current loss. Leonardi et al. (1996) proposed a FEM technique for iron loss calculation in synchronous reluctant machines.

Finally, Kaido (1991) developed a mechanical method of iron loss measurement in a rotational field measured from induced torque and Stranges and Findlay (2000) developed a method for measuring rotational iron loss in electrical sheet and results obtained show that higher portion of the total iron loss is due to hysteresis.

2.3.2 Effect of Stresses on Iron Loss

The studies of the dependence of iron losses on mechanical stresses have been a research of interest in the analysis of iron core loss computation. Some of the investigations which study the effect of stresses on iron core losses are reviewed here.

Foster (1984) studied the B^{γ} dependence of the hysteresis losses of several electrical steels over a flux density range of 0.4 T to 1.7 T as a function of applied stress up to 7 MPa. Foster found that γ increases from 1.6 up to 2 for regular grain oriented (RGO) and high permeability oriented (HGO) steel and up to 1.8 for non-oriented silicon sample. The effect of radial compressive stress on flux distribution and power loss was demonstrated on two different non-oriented low silicon stator cores of an induction motor by Moses and Rahmatizadeh (1989). Moses found by applying 4 MPa stress on the stator lamination changes in the flux distribution which increases local loss mostly behind the stator teeth. Ali et al. (1997) developed a technique for predicting the effect of mechanical stress on the iron loss density of laminated core under alternating flux condition. Ali's work revealed that the iron loss density is most sensitive to the compressive stress, particularly at low flux density.

LoBue et al. (1999) and Permiakov et al. (2002, 2004) studies the effect of tensile and compressive stress on power losses of Fi-Si non-oriented electrical steels in agreement with the statistical theory of loss separation. The losses calculation by LoBue were done by means of the Dynamic Preisach Model and measurements were made for stress ranges -50 MPa to 50 MPa under controlled sinusoidal induction (0.5, 1.0, and 1.5 T) at 200 Hz. LoBue found that the hysteresis loss and excess loss components increase drastically for applied compressive stress while tensile stress causes some reduction in the losses.

Similarly, Permiakov investigated the variation of the hysteresis and excess losses described by the hysteresis energy loss W_h and material parameter V_0 respectively, at applied uniaxial compressive and tensile elastic stresses and up to plastic deformation under sinusoidal flux. The dependence of the hysteresis and excess loss on elastic

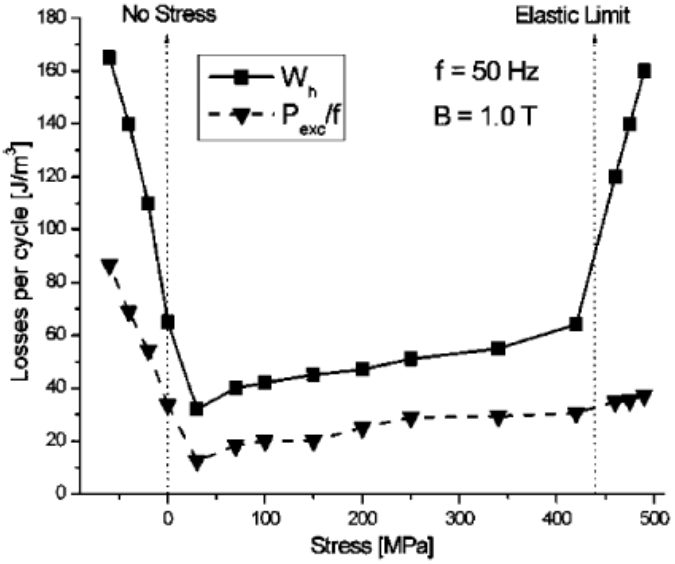

Figure 2: Hysteresis loss (W_h) and excess loss per cycle versus stress. (Permiakov et al., 2004).

stress was found to be similar as depicted in Figure 2. The hysteresis and excess loss increases drastically as compressive stress increase while at plastic deformation all components of losses increase drastically.

2.4 Magnetization Curve, Hysteresis loop and Stress

The magnetization curve of ferromagnetic materials has a fundamental importance of describing the magnetic properties of the material. It is obtained by plotting the intensity of magnetization I or the flux density B against the field strength H. The behavior of ferromagnetic materials is also described by the permeability curve and hysteresis loop. The permeability is described as the increase in flux caused by the presence of magnetic material (Bozorth, 1993). The value of the field strength at the negative magnetic field for which flux density is zero is the coercive force H_c and the value of the flux density for which field strength is zero is the remanence or residual flux density B_r. Figure 3 shows a family of hysteresis loops with the magnetization curve (dash-lines) emerging from the locus of the tip of the hysteresis loop.

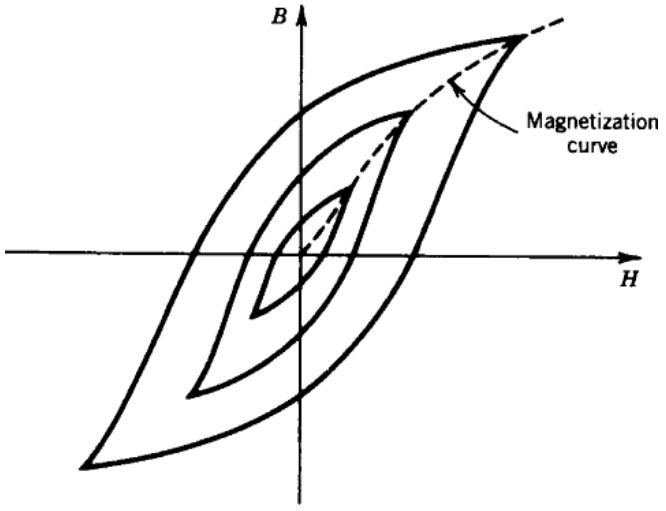

Figure 3: Magnetization curve and hysteresis loop. (Sen, 1997).

It is known that electrical iron sheets are subjected to mechanical stresses which may result from manufacturing processes and operational processes for rotating electrical machines. These stresses are known to affect the magnetic properties of the electrical iron sheet material. In recent years, several researchers have investigated the effect of mechanical stresses on the BH-curve and hysteresis loop. These researchers have greatly unfolded the importance of the knowledge of the total mechanical stress distribution in an electrical machine core. Some of these are reviewed.

Yamamoto et al. (1998) studied the effect of shrink fitting (SUS304 stainless steel (SUS) and aluminium (Al) frame) on magnetic properties of electrical iron core. It was found that the compressive stressed induced by shrink fitting decreases the permeability and increases the magnetic losses; explained by the increase of the magneto-elastic energy due to compressive stress due to shrink fitting. Figure 4 shows the results of Yamamoto's investigation for magnetization and hysteresis curves behavior due to shrink fitting. The Young's Modulus for Al and SUS are

7.03×10^{10} Pa and 19.0×10^{10} Pa respectively. These results are in agreement with LoBue et al. (1999) calculation done by means of Dynamic Preisach Model which studies the effect of applied external stress on dynamic hysteresis loop for Si-Fe non-oriented lamination.

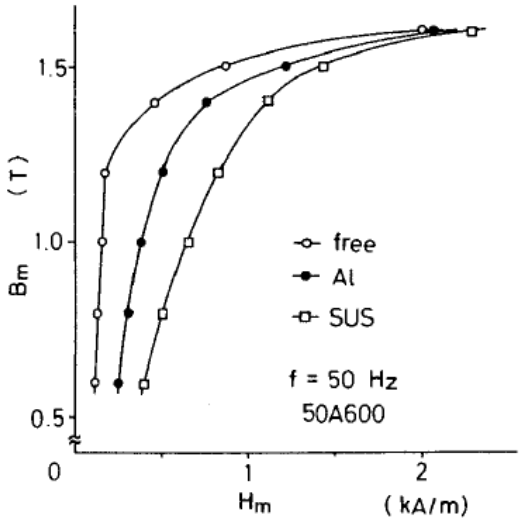

(a) Magnetization curve

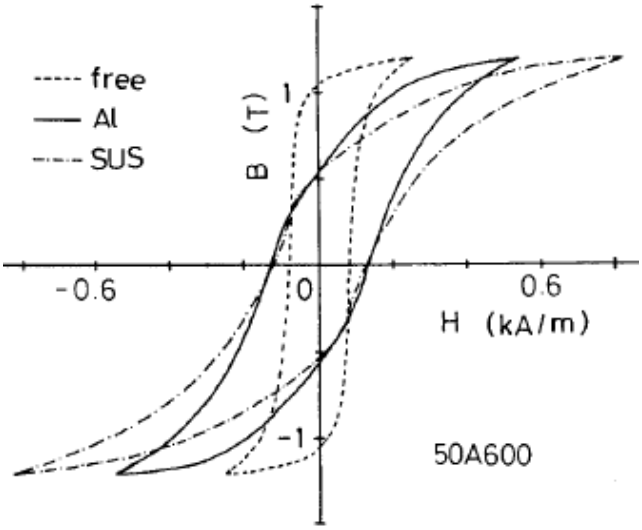

(b) Hysteresis curve

Figure 4: Magnetic properties of iron core before and after shrink fitting (Yamamoto et al., 1999)

Permiakov et al. (2002, 2003) investigated the effect of a range of unidirectional applied mechanical stresses on the magnetic properties of non-oriented Fe-Si electrical steel under sinusoidal and distorted excitation. They found that at increasing compressive stress the distorted BH-loops gradually become wider. Similar behavior was also obtained at increasing plastic strain for both distorted and sinusoidal

BH-loops. The measurements conducted by Pulnikov et al. (2003) which study the effect of applied tensile stresses on magnetic properties of Fe-Si non-oriented electrical steel show a gradual increase in the coercive field for increasing stresses and a considerable rise at plastic deformation which agrees with the work by LoBue et al. (1999).

The behavior of the relative permeability of $35A360$ grade non-oriented electrical steel sheet under compressive stress up to -150 MPa was investigated by Takahashi and Miyagi (2008) and Miyagi et al. (2010). They found that the permeability decreases rapidly even at small stress rate in both the rolling and transverse directions, while for stress larger than -50 MPa, the material anisotropy disappears. The increase in coercivity due to stress causes an increase in the hysteresis loss.

2.5 Coupled Magneto-mechanical Analysis

Coupled problems involve interaction of two or more interconnected phenomena either simultaneously or by post-processing. Coupled magneto-mechanical analysis in electrical machines is primarily concerned with the interaction between the magnetic and mechanical fields problem. This presents problematic matters related to stresses occurring or existing in rotating electrical machine lamination. These could be electromagnetic forces, vibrations and noise from magnetostriction: the effect of dimension change of substance when subjected to magnetic field.

2.5.1 Magneto-mechanical Coupling Methods

The solving of magnetic and mechanical problems have been implemented using different coupling methods by different authors in past research. In view of modeling, material or structural behavior which defines different physical phenomena can be modeled based on the objectives and goals of the model either as coupled or uncoupled. These phenomena can also be classified either as *global* or *local* coupling.

The global coupling involves the conservative laws and set boundary conditions. The coupling consists of coupled field solutions with or without constitutive equations. On the other hand, the local coupling consists of coupled constitutive equations of the materials; it requires a clear insight of the different microscopic mechanisms responsible for the microscopic behavior of the materials during the interaction between the magnetic and mechanical phenomena. The numerical implementation of these methods within the framework of finite-element-method has been exemplified by (Hirsinger and Billardon, 1995).

The global and local coupling method was implicitly applied by Belahcen (2005) to study the effect of magnetoelastic coupling on the vibration of the stator core of a synchronous generator. Belahcen found that there is a 20 % increase in the vibration when compared to an uncouple problem. The local magneto-mechanical coupling method was implemented by Belahcen and Arkkio (2006) as a stress dependency of magnetization properties of lamination for an induction machine. The efficiency of the machine was reduced; as such they suggested the need for bidirectional stresses and measurement under rotating flux density for better computational accuracy.

Coupling can also be described as *direct* or *indirect*. Coupling is achieved using iterative schemes which depends on the problem intricacy and formulated equations.

2.5.1.1 Direct Coupling

A direct coupling involves solving the magnetic and mechanical equations simultaneously by suitable dependencies. Knowledge of the interaction of the different governing materials behavior is required, this is illustrated by the flowchart in Figure 5c. This method was implemented in the simulation of the effect of magnetostriction and electromagnetic stress in iron by (Fonteyn et al., 2010a), focusing on the

suitability of the technique for vibration analysis in electrical machines. The 2-D magnetic field and displacement were solved simultaneously without the use of common "equivalent forces" approach. The accuracy of this method was validated experimentally by Fonteyn et al. (2010b): it was implemented numerically to simulate the magneto-mechanical effect which study the actual influence of the Maxwell stress tensor within iron cores.

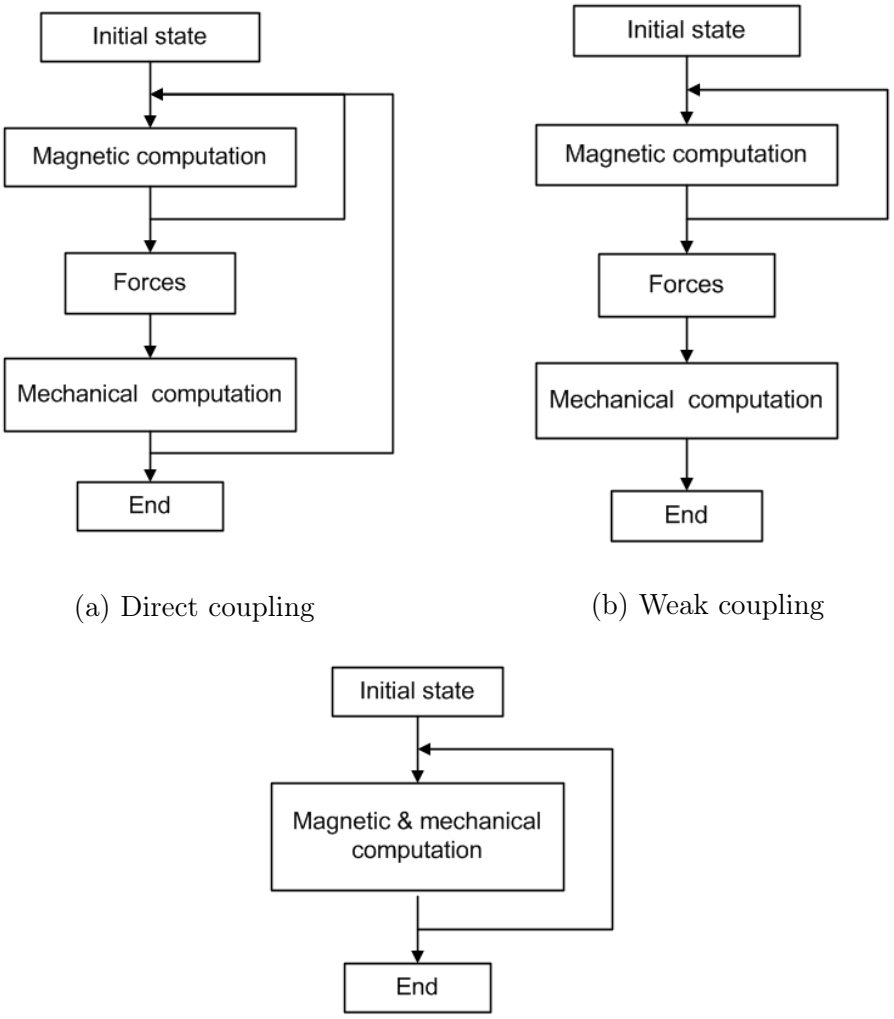

(a) Direct coupling

(b) Weak coupling

(c) Strong coupling

Figure 5: Flow chart for different coupling methods.

2.5.1.2 Indirect Coupling

In indirect coupling, the magnetic, mechanical and other properties of the materials are not in direct relationship to each other: these could either occur when the dependency between these properties is very small and is ignored or the exact relationship

between the properties is not known. Coupling between fields can still be done if coupling between material properties is ignored. Indirect coupling are either a *weak* or *strong* coupling.

Weak Coupling

In weak coupling, the effect of one field solution on another is unidirectional as demonstrated in Figure 5b for a magneto-mechanical coupling. This method is quite commonly used in conventional electrical machine designs. In this case, the solved magnetic properties are used as input for the mechanical problem, but not the other way around. The magnetic forces obtained from the solved magnetic field are set as applied load in the mechanical analysis problem; and the solved mechanical problem has no backward effect on the magnetic properties of the material.

The implementation of weak coupling in problem solving is usually done by a computer program. The magnetic field computation is first established from initial conditions. From the field solution, the magnetic forces could be obtained by one of the force computation method listed in Section 2.1.1. The forces obtained by the magnetic analysis are then used as input in another computer program where the mechanical problems are solved; this gives the displacement field from which other quantities are obtained.

Belahcen (2004) implemented this method to compute the vibration of the stator core in rotating electrical machine under the effect of magnetic and magnetostrictive forces.

Strong Coupling

In strong coupling, the effect of the magnetic field is taken into account in the mechanical analysis and the effect of the mechanical field is also considered in the magnetic field analysis; this method is demonstrated by the flowchart in Figure 5a. This type of computation is implemented mostly in cases where the mechanical stresses are so large that it can cause a change in the magnetic properties of the electrical machine material. Researches which implemented this methods in magneto-mechanical problems solving are reviewed here.

In the analysis of magneto-mechanical problems, Besbes et al. (1996) implemented a strongly coupled method in the computation of the magnetic force in a magnetostrictive material by virtual work principle. Gros et al. (1998) implemented this method in the modelling of a magnetostrictive actuator, and for the reduction of CPU time with respect to iterative processes. Yang et al. (2006) studied a magneto-mechanical strongly coupled model to accurately calculate the performance of a force sensor with giant magnetostrictive material and the results obtained was in agreement with that of measurements.

3 Methodology

In this section the methods implemented in the study of the mechanical stress distribution in a synchronous reluctance machine model are discussed. This work focuses on the mechanical stresses due to shrink fit, centrifugal forces and the magnetic forces acting on a synchronous reluctance machine. The stresses due to shrink fitting from the manufacturing process is a static stress type, while stresses resulting from the centrifugal forces and the magnetic forces are dynamic stresses and only exist when the machine is fed from a source and running.

The combined effect of the stresses could be obtained analytical by superposition method; achieved by solving the separate stresses and summing up the total stress components. To study the stresses due to shrink fitting and centrifugal forces, an approximate expression was obtained for calculating the radial and tangential stress distribution acting on a simple shrink fitted cylindrical geometry without rotor and stator slots. Since it is difficult to compute the stress due to magnetic field analytically as a result of the complex geometry of the synchronous reluctance machine, the stresses due to magnetic forces were only computed by finite-element method.

The numerical analysis was implemented in finite-element commercial software (COMSOL Multiphysics). The stress due to shrink fitting and centrifugal forces were computed based on the principle of solid mechanics, while the magnetic analysis was obtained based on the principle of electromechanics. The magnetic forces obtained in the magnetic analysis were weakly coupled to the solid-mechanics displacement field of the geometry to give the combined stress distribution. The interaction between the magnetic analysis and mechanical analysis (displacement field or stresses) in this investigation is unidirectional; this study the effect of the magnetic field on the mechanical field but not the mechanical field on the magnetic field or properties.

To begin this analysis, a step-by-step approach used in the analytical computation of the stresses due to shrink fit and centrifugal forces is described. Furthermore, the methods used in the numerical analysis of the mechanical and magnetic field computation in this study are discussed here.

3.1 Analytical Method of Mechanical Stress

3.1.1 Shrink Fitting

Shrink fitting is a manufacturing process which involves overlapping one cylinder over another. This is usually accomplished by fitting an outer cylinder with inner diameter c onto another cylinder of outer diameter slightly larger than its inner diameter after expending the outer cylinder by heating or shrinking the inner cylinder by cooling to freezing temperature. Figure 6 depict the amount δ by which the outer diameter of the inner cylinder is larger than the inner diameter of the outer cylinder. This extra radial length on the inner cylinder is known as the $radial\ interference$.

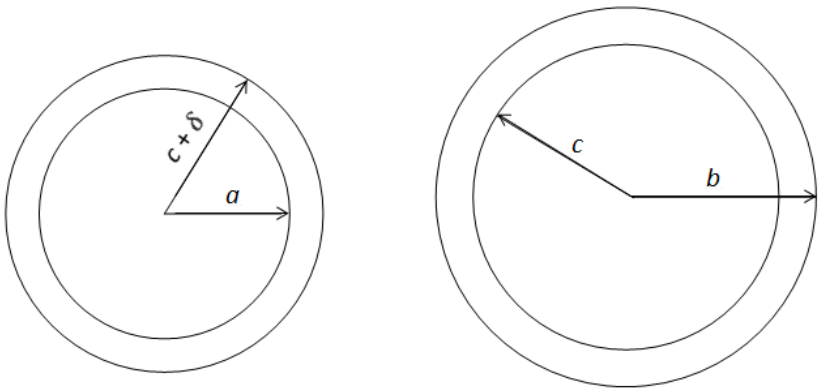

Figure 6: Shrink fit geometries for inner (left) and outer (right) cylinder.

The theoretical approximation used in the analytical calculation of the mechanical stresses due to shrink fitting are given in (Bickford, 1998). The equations are used in the stress calculation due to shrink fitting on a compound cylindrical geometry due to a condition known as $plane-strain$. In this condition, the rotor and stator of the synchronous reluctance machine are considered as cylinders in which the stresses in the axial direction are radially dependent $\sigma_z(r)$, thus preventing any axial displacement $w = 0$: this implies that the strain in the z-direction $\epsilon_z = 0$. The condition for considering the plane–strain holds when the z–dimension or length of the electrical machine is large when compared with outer radius of the cylinder.

The synchronous reluctance machine as in many other rotating electrical machines is made of a solid shaft, rotor core, stator core and a body frame. The frame of an electrical machine can be an Aluminium or Cast iron Frame. The equation which describes the radial and circumferential stress in a cylindrical geometry is given by

$$\sigma_{\mathrm{r}} = \frac{E}{(1+\upsilon)(1-2\upsilon)}\mathrm{C_i} - \frac{E}{1+\upsilon}\frac{\mathrm{C_j}}{r^2} = \mathrm{A} - \frac{\mathrm{B}}{r^2} \tag{3.1}$$

$$\sigma_{\theta} = \frac{E}{(1+\upsilon)(1-2\upsilon)}\mathrm{C_i} + \frac{E}{1+\upsilon}\frac{\mathrm{C_j}}{r^2} = \mathrm{A} + \frac{\mathrm{B}}{r^2} \tag{3.2}$$

Where r is the radius, $\mathrm{C_i}$ and $\mathrm{C_j}$ are constants, while σ_r and σ_c are the radial and circumferential stresses in a cylinder respectively. A and B in the expression at the right hand side of (3.1) and (3.2) are also arbitrary constants; the expression is known as the Lamé's equation discussed in Section 2.2.2. The equation which defines the displacement in the cylindrical core obtained in (Bickford, 1998) is given as

$$u = \mathrm{C_i}r + \frac{\mathrm{C_j}}{r} \tag{3.3}$$

To obtain an approximate expression for shrink fitting between the rotor-shaft and the stator-frame interface, the following assumptions were considered:

(a) There are no symmetric temperature and body force inputs.

(b) The core materials of the shrink-fitted geometry are linearly elastic and isotropic materials.

The theoretical expressions obtained for the computation of the radial and circumferential stress distribution due to the rotor-shaft and stator-frame shrink fitting are discussed in the following section.

3.1.1.1 Shaft-Rotor Fit

The expression for mechanical stress calculation due to shrink fit between the shaft and rotor core is obtained using the expression (3.1) and (3.2) for both the shaft and rotor core. If we assume both geometries to be cylindrical tubes as shown in Figure 6, and for the shaft the value of $a = 0$ which demands that $\mathrm{C_2}$ must be zero so that the displacement u is not infinity. The boundary conditions at the interface are

Interface: $\sigma_{\mathrm{ri}}(c) = \sigma_{\mathrm{ro}}(c)$ and $u_{\mathrm{o}} - u_{\mathrm{i}} = \delta$

Outer boundary: $\sigma_{\mathrm{ro}}(b) = 0$

Where σ_{ri} and σ_{ro} are the radial stresses at the interface of the inner and outer cylinder respectively. u_{i} and u_{o} are the displacement at the interface of the inner and outer cylinder respectively. The equations for the stresses are

$$\sigma_{\mathrm{ri}} = \frac{E_{\mathrm{i}}}{(1+\upsilon_{\mathrm{i}})(1-2\upsilon_{\mathrm{i}})}\mathrm{C}_1 \tag{3.4a}$$

$$\sigma_{\theta i} = \frac{E_{\mathrm{i}}}{(1+\upsilon_{\mathrm{i}})(1-2\upsilon_{\mathrm{i}})}\mathrm{C}_1 \tag{3.4b}$$

Where σ_{ri} and $\sigma_{\theta i}$ are the equations for the radial and circumferential stress distribution in the solid shaft (inner tube). In the case of the rotor core (outer tube), the equations for the radial and circumferential stress distribution are

$$\sigma_{\mathrm{ro}} = \frac{E_{\mathrm{o}}}{(1+\upsilon_{\mathrm{o}})(1-2\upsilon_{\mathrm{o}})}\mathrm{C}_3 - \frac{E_{\mathrm{o}}}{(1+\upsilon_{\mathrm{o}})}\frac{\mathrm{C}_4}{r^2} \tag{3.5a}$$

$$\sigma_{\theta o} = \frac{E_{\mathrm{o}}}{(1+\upsilon_{\mathrm{o}})(1-2\upsilon_{\mathrm{o}})}\mathrm{C}_3 + \frac{E_{\mathrm{o}}}{(1+\upsilon_{\mathrm{o}})}\frac{\mathrm{C}_4}{r^2} \tag{3.5b}$$

The expressions for the constants in the above expression are given in Appendix A.

3.1.1.2 Stator-Frame Fit

Similar procedure implemented in the preceding section also applies here. In addition, since we have a hollow inner cylinder as shown in Figure 6. The boundary conditions for solving the expression of the radial and circumferential stresses becomes

Inner boundary: $\sigma_{\mathrm{ri}}^{st}(a) = 0$

Interface: $\sigma_{\mathrm{ri}}^{st}(c) = \sigma_{\mathrm{ro}}^{st}(c)$ and $u_o - u_i = \delta$

Outer boundary: $\sigma_{\mathrm{ro}}^{st}(b) = 0$

From the above boundary conditions the following expressions for the mechanical stresses due to shrink fitting on the stator-frame interface are obtained

$$\sigma_{\mathrm{ri}}^{st} = \frac{E_{\mathrm{i}}}{(1+\upsilon_{\mathrm{i}})(1-2\upsilon_{\mathrm{i}})}\mathrm{C}_5 - \frac{E_{\mathrm{i}}}{(1+\upsilon_{\mathrm{i}})}\frac{\mathrm{C}_6}{r^2} \tag{3.6a}$$

$$\sigma_{\theta i}^{st} = \frac{E_{\mathrm{i}}}{(1+\upsilon_{\mathrm{i}})(1-2\upsilon_{\mathrm{i}})}\mathrm{C}_5 + \frac{E_{\mathrm{i}}}{(1+\upsilon_{\mathrm{i}})}\frac{\mathrm{C}_6}{r^2} \tag{3.6b}$$

.
Where $\sigma_{\mathrm{ri}}^{st}$ and $\sigma_{\theta i}^{st}$ are the equations for the radial and circumferential stress distribution at the stator core (inner tube). In the case of the Frame (outer tube), the equations for the radial and circumferential stress distribution are

$$\sigma_{\mathrm{ro}}^{st} = \frac{E_{\mathrm{o}}}{(1+\upsilon_{\mathrm{o}})(1-2\upsilon_{\mathrm{o}})}\mathrm{C}_7 - \frac{E_{\mathrm{o}}}{(1+\upsilon_{\mathrm{o}})}\frac{\mathrm{C}_8}{r^2} \tag{3.7a}$$

$$\sigma_{\theta o}^{st} = \frac{E_{\mathrm{o}}}{(1+\upsilon_{\mathrm{o}})(1-2\upsilon_{\mathrm{o}})}\mathrm{C}_7 + \frac{E_{\mathrm{o}}}{(1+\upsilon_{\mathrm{o}})}\frac{\mathrm{C}_8}{r^2} \tag{3.7b}$$

The expressions obtained in this section are all cases of static stress calculation and they are also valid for the computation of any compound cylindrical geometry under the effect of shrink fit bounded by the assumptions stated earlier in this section. The expressions for the constants in the above expression are given in Appendix A.

3.1.2 Stress due to Centrifugal Force

In operational rotating electrical machines, the rotor and shaft are subject to rotational motion from the rotating magnetic field. This rotational speed generates a force on the rotating parts known as *centrifugal force*. To obtain the mechanical stress distribution due to centrifugal force by analytical method, the effect of the rotational speed is included in the calculation. The equation which defines the force acting on a cylindrical body having a rotational speed ω and density ρ as shown in Figure 7 is given by

$$F_c = \omega^2 \rho r \tag{3.8}$$

The equations for the radial displacement of a cylindrical tube governed by the assumption stated in the previous section and rotating at rotational speed ω are given by

$$\begin{aligned} u_{\mathrm{i}} &= \mathrm{C}_9 r + \frac{(2\upsilon_{\mathrm{i}}-1)}{8E_i(\upsilon_{\mathrm{i}}-1)^2}\rho_{\mathrm{i}}\omega^2 r^3 \\ u_{\mathrm{o}} &= \mathrm{C}_{11} r + \frac{\mathrm{C}_{12}}{r} + \frac{(2\upsilon_{\mathrm{o}}-1)}{8E_o(\upsilon_{\mathrm{o}}-1)^2}\rho_{\mathrm{o}}\omega^2 r^3 \end{aligned} \tag{3.9}$$

The boundary conditions are give below

Interface: $\sigma_{ri}^*(c) = \sigma_{ro}^*(c)$ and $u_o - u_i = 0$

Outer boundary: $\sigma_{ro}^*(b) = 0$

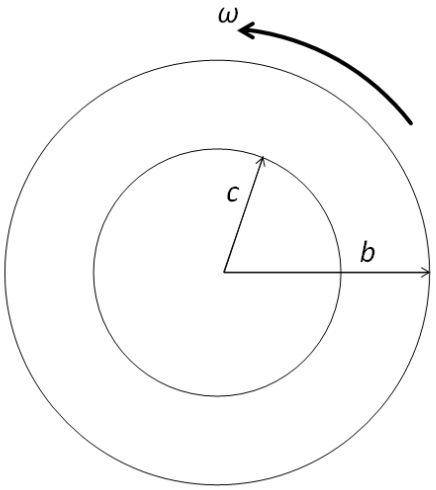

Figure 7: Rotating rotor-shaft assembly at constant rotational speed ω.

The equations for the radial and circumferential stress distribution given in (Bickford, 1998) for a shaft-tube compound cylinder at rotational speed ω are given by

$$\sigma_{ri}^{*} = \frac{E_{\mathrm{i}}}{(1+\upsilon_{\mathrm{i}})(1-2\upsilon_{\mathrm{i}})}\mathrm{C}_9 + \frac{\rho_{\mathrm{i}}\omega^2 r^2}{8}\left(\frac{1}{\upsilon_{\mathrm{i}}-1} - 2\right) \tag{3.10a}$$

$$\sigma_{\theta i}^{*} = \frac{E_{\mathrm{i}}}{(1+\upsilon_{\mathrm{i}})(1-2\upsilon_{\mathrm{i}})}\mathrm{C}_9 + \frac{\rho_{\mathrm{i}}\omega^2 r^2}{8}\left(\frac{3}{\upsilon_{\mathrm{i}}-1} + 2\right) \tag{3.10b}$$

$$\sigma_{ro}^{*} = \frac{E_{\mathrm{o}}}{(1+\upsilon_{\mathrm{o}})(1-2\upsilon_{\mathrm{o}})}\mathrm{C}_{11} - \frac{E_{\mathrm{o}}}{(1+\upsilon_{\mathrm{o}})}\frac{\mathrm{C}_{12}}{r^2} + \frac{\rho_{\mathrm{o}}\omega^2 r^2}{8}\left(\frac{1}{\upsilon_{\mathrm{o}}-1} - 2\right) \tag{3.10c}$$

$$\sigma_{\theta o}^{*} = \frac{E_{\mathrm{o}}}{(1+\upsilon_{\mathrm{o}})(1-2\upsilon_{\mathrm{o}})}\mathrm{C}_{11} + \frac{E_{\mathrm{o}}}{(1+\upsilon_{\mathrm{o}})}\frac{\mathrm{C}_{12}}{r^2} + \frac{\rho_{\mathrm{o}}\omega^2 r^2}{8}\left(\frac{3}{\upsilon_{\mathrm{o}}-1} + 2\right) \tag{3.10d}$$

The values of the the constants used in the analytical calculation of the mechanical stress distribution are give in Appendix A.

3.1.3 Total Stress due to Shrink fit and Centrifugal force

The total mechanical stress due to shrink fitting from the static stress and the dynamic centrifugal stress are obtained by summing the individual stress components of the rotational parts. This is because that mechanical stress obeys the law of superposition. Therefore, the total mechanical stresses acting on the shaft are given by

$$\begin{aligned} \sigma_{\mathrm{ri}}^{\mathrm{t}} &= \sigma_{\mathrm{ri}} + \sigma_{\mathrm{ri}}^{*} \\ \sigma_{\theta\mathrm{i}}^{\mathrm{t}} &= \sigma_{\theta\mathrm{i}} + \sigma_{\theta\mathrm{i}}^{*} \end{aligned} \tag{3.11}$$

Similarly, the total mechanical stresses acting on the rotor core are given by

$$\begin{aligned} \sigma_{\mathrm{ro}}^{\mathrm{t}} &= \sigma_{\mathrm{ro}} + \sigma_{\mathrm{ro}}^{*} \\ \sigma_{\theta\mathrm{o}}^{\mathrm{t}} &= \sigma_{\theta\mathrm{o}} + \sigma_{\theta\mathrm{o}}^{*} \end{aligned} \tag{3.12}$$

These expressions give the total mechanical stress distribution of a rotating electrical machine subjected to shrink fitting and centrifugal forces in the radial and circumferential direction.

3.2 2-D FE-Analysis of Sychronous Reluctance Machine

In this section, the methodology implemented in the two-dimensional finite–element analysis of the mechanical stress computation are discussed. The various design tools used and the methods applied in the achievement of the goal and objective of this project are presented. The dimension of the synchronous machine type, machine parameters and the material properties are important input in this analysis.

The aim of this work as stated earlier is to study the two–dimensional mechanical stress distribution due to shrink fitting from the manufacturing issues, centrifugal forces resulting from the rotating rotor and shaft body mass and the magnetic forces from the rotating magnetic field of the synchronous reluctance machine at 50 Hz. The study also shows how changes in the radial interference dimension in the shrink fitted parts affect the mechanical stress distribution. Furthermore, the effect of the rotational speed on the stress distribution at different frequencies was computed. The data obtained were ad hoc for comparing for the different stress parameters.

The machine investigated is a 400 V, 37 kW three-phase synchronous reluctance machine at 50 Hz. The importance of this study is in prediction of the mechanical stresses distribution. This stresses are known to have adverse effect on the magnetic properties of electrical iron sheet. This analysis presents the effects of the various conditions under study on the synchronous reluctance machine and the combined stresses.

Model building

The numerical analysis was implemented using commercial finite-element software (COMSOL Multiphysics). The 2-D model to be analyzed was created using Pro/Engineer software and then imported to the COMSOL Multiphysics for the numerical investigation to be carried out.

Table 1: The main dimensions of the SynRM

Dimensions	[mm]	Dimensions	[mm]
D21	198.5	D_{S1}	310.0
D22	60.0	D_{S2}	200.0
H0	10.0	H1	23.9
H01	2.5	H11	1.0
B01	6.0	H13	17.5
B02	2.0	B11	3.5
B03	8.0	B12	6.5
B04	2.50	B13	8.8
l_r	246	D_{F1}	310
l_s	246	D_{F2}	350

The main dimensions of the machine are given in Table 1, The slot type for this synchronous reluctance machine is shown in Figure 8 and 9. The cross-section of the 2-D geometry of the synchronous reluctance machine under study is shown in Figure 10a.

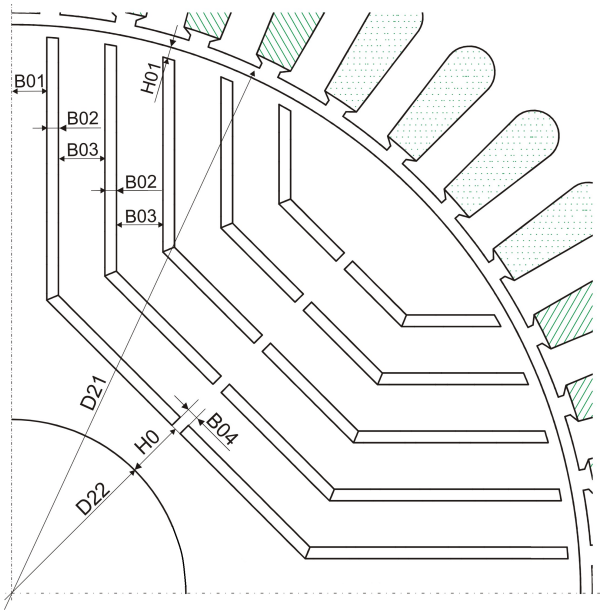

Figure 8: Dimension of rotor geometry.

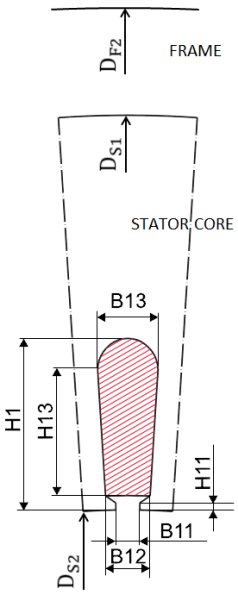

Figure 9: Stator slot and frame dimensions.

Machine Parameters

The machine under study is a 400 V, 37 KW three-phase star-connected synchronous reluctance machine with a rotational speed of 1500 rpm. The rated machine parameters are given in Table 2. Based on the torque obtained from the simulation in Section 3.2.3, the maximum and minimum radial interference δ in the shrink fitted were obtained in compliance with the interference fit standard (DIN 7190, 2001). The maximum value of δ was obtained based on the rated torque value of the machine, while the minimum value is that value for which there is no slip in the fitted contact.

The rotor and stator core are made of electrical steel lamination, the shaft is a structural steel grade while the frame is an alloy of Aluminium (Aluminum 6061). The various properties of the synchronous reluctance machine materials used in this FEM analysis are presented in Appendix B. The rated parameters of the synchronous reluctance machine are obtained by simulation using in-house software (FCSMEK). The data obtained are given in Table 2; these are used as input in the magneto-mechanical analysis. The simulation procedure is presented in Section 3.2.3.

Table 2: The SynRM machine parameters

Machine parameters	Values
Power	37 kW
Voltage	400.0 V
Current	79.0 A
Frequency	50 Hz
Power factor	0.5768 Ind.
Connection	Star
Rotation angle	-40 Elec. deg.

3.2.1 FEM Simulation in COMSOL Multiphysics

The pre-processing and post-processing of numerical computation of the mechanical stresses was implemented in COMSOL Multiphysics. To begin FEM analysis of the machine, a 2-D CAD model of the machine was created using Pro/Engineer CAD tool. The model was then imported to COMSOL Multiphysics; where the numerical analysis was carried out.

The model was slightly modified by creating contact pairs interface for the shrink fitting study. These contact pairs define the rotor-shaft and stator-frame interface with an overlapping radial length equal to δ. This permits the implementation of the value of δ in stress calculation. It should be noted that in this simulation, the computation of the mechanical stress distribution due shrink fitting is not dependent on the contact pressure at the interface, rather it is dependent on the radial

interference at the contact interface as shown in Figure 6.

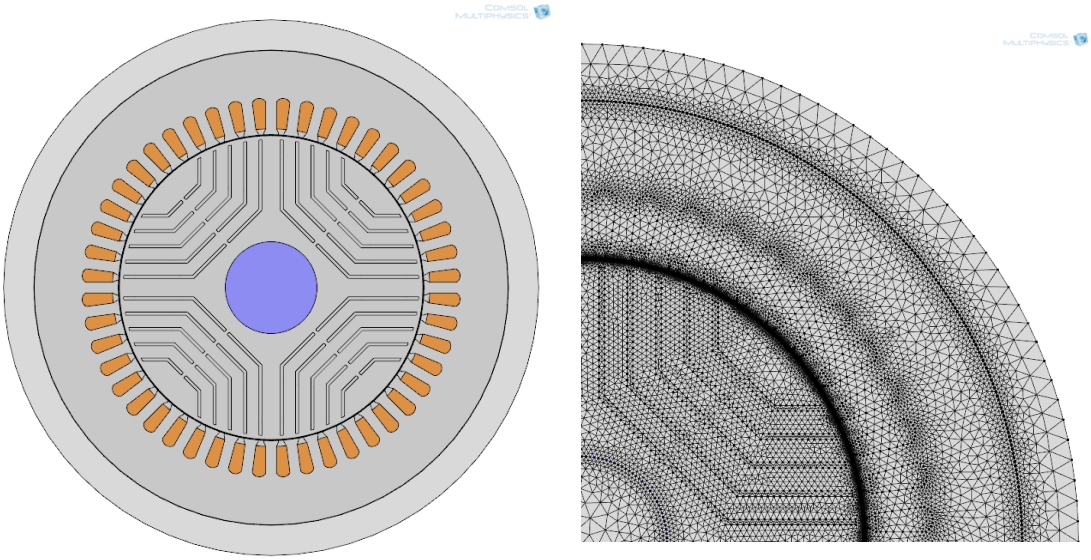

(a) The SynRM model

(b) The SynRM mesh

Figure 10: Machine geometry and mesh.

The numerical analysis of the mechanical stress distribution was done in two stages. The first stage computed the mechanical stress due to shrink fitting and centrifugal force using a mechanical analysis approach. The computation was carried out in a solid-mechanics physics interface. The solutions were the stresses, strain and displacement field of the structural geometry. The second stage is a magnetic analysis of the system. It was done in the rotating-machinery-magnetic physic and the solutions of this analysis are the vector potential from which the magnetic forces were obtained.

The solution of the electromechanical computation was obtained based on a weakly coupled approach. In this approach, the results from the magnetic field computation were used as input for the mechanical analysis, but the results of the mechanical analysis have no effect on the magnetic field computation.

3.2.2 Shrink Fitting and Centrifugal Force

The shrink fit computation was carried out using solid-mechanics physics in COMSOL Multiphysics. In the mechanical analysis, the following assumptions were taken into consideration: The model is computed in a 2-D plane-strain condition, the material is isotropic and all the contact boundaries are considered initially free. The shrink fit interfaces were modeled as an assembly of two free interfaces which overlap at the contact pairs. The equation which defines the solid-mechanics physics is given by

$$-\nabla \cdot \sigma = \boldsymbol{F}_V \tag{3.13}$$

Where σ is the stress while $\boldsymbol{F}_V$ is the volume force density. The displacement and deformation of each domain resulting from the stresses are defined by 3.13 – 3.15. Since shrink fitting is a manufacturing process and we are considering the effect of the radial interference, the effect of the temperature changes due to the expansion or shrinking of the machine parts are neglected. The dependent variable used in this computation is the radial interference (interference displacement) given as δ_{sr} and δ_{sf} for the rotor-shaft and stator-frame respectively.

The linear elastic properties of the materials in the analysis are defined by equation 3.13, while equations (3.14) and (3.15) give the total strain tensor in terms of the displacement gradient and the Duhamel-Hooke's law which relates the stress tensor to the strain tensor and temperature. These equations are

$$\epsilon = \frac{1}{2}\left[(\nabla \boldsymbol{u})^T + \nabla \boldsymbol{u} + (\nabla \boldsymbol{u})^T \nabla \boldsymbol{u}\right] \tag{3.14}$$

$$s - s_0 = C : \left(\epsilon - \epsilon_0 - \epsilon_{inel}\right) \tag{3.15}$$

where s_0 and ϵ_0 are the initial stress and strain respectively. C is the 4th order elasticity tensor, $\boldsymbol{u}$ is displacement and ":" stands for the double-dot tensor product. The variable $\epsilon_{inel} = \alpha\theta$ and $\theta = T - T_{\text{ref}}$, where α is the thermal expansion tensor and T and T_{ref} are the current and reference temperature respectively.

The material properties were defined for each domain of the electrical machine model. For the solid parts of the machine under study, the material properties were defined based on the linear elastic material properties as expressed by equations 3.13 – 3.14. The shrink fitted interfaces were defined as contact pairs for both the rotor-shaft and stator-frame domain. The initial contact pressure for the analysis was assumed to be zero. The domains surrounded by air were isolated in the solid-mechanics analysis because air has no role in this stress computation.

To simulate the effect of the centrifugal forces on the rotating rotor domain, a body load boundary was used to set a body force on the shaft and rotor domain. The body force density which defines the body load of the rotating shaft and rotor domain is defined by the centrifugal force given by

$$F_{\text{c}} = \rho\omega^2 r \tag{3.16}$$

Where ρ, ω and r are the density, rotational speed and the radius of the rotating body.

The mesh of the synchronous reluctance machine used in the finite-element analysis is fine at the contact boundaries and normal at the rest of the machine domains. This is shown in Figure 10b.

In order to obtain a better understanding of the behavioral characteristic of the mechanical stresses in the synchronous reluctance machine geometry, a study was conducted for various values of δ at both the rotor-shaft and stator-frame interfaces. The minimum value of the radial interference would only prevent the contact from sliding and slipping. The maximum radial interference was obtained from the rated torque defined in (DIN 7190, 2001). A parametric sweep was carried out for five different values of the radial interference. The values of the radial interference obtained and the corresponding contact pressure are given in Table 3.

The analysis was also conducted to study the stress distribution due to centrifugal forces at frequencies; 75 Hz and 100 Hz respectively. This gave an insight on how the stresses change with increasing rotational speed or increasing centrifugal forces. The results of analysis are presented in section 4.

Table 3: Interference displacement and contact pressure

Shaft–rotor δ_{sr}	Max. contact pressure
$4.181 \cdot 10^{-4}$ (mm)	1.0 MPa
$8.481 \cdot 10^{-3}$ (mm)	19.6 MPa
$1.654 \cdot 10^{-2}$ (mm)	38.2 MPa
$2.461 \cdot 10^{-2}$ (mm)	56.8 MPa
$3.267 \cdot 10^{-2}$ (mm)	75.4 MPa
Stator–frame δ_{sf}	Max. contact pressure
$1.090 \cdot 10^{-3}$ (mm)	0.05 MPa
$6.978 \cdot 10^{-2}$ (mm)	3.4 MPa
$1.385 \cdot 10^{-1}$ (mm)	6.7 MPa
$2.072 \cdot 10^{-1}$ (mm)	10.0 MPa
$2.758 \cdot 10^{-1}$ (mm)	13.4 MPa

3.2.3 Magnetic Forces Computation

To investigate the mechanical stress distribution due to magnetic forces in the synchronous reluctance machine, we use the machine parameters obtained from the simulation done in the in-house software (FCSMEK). The physical values of the synchronous reluctance machine used in the simulation are given in the file *cim.data*; this is given in Appendix C. The simulations follow the steps on the flowchart shown in Figure 11

The first simulation step generates the mesh of the synchronous reluctance machine, this was executed by using the program command $MESH$. The second step was ex-

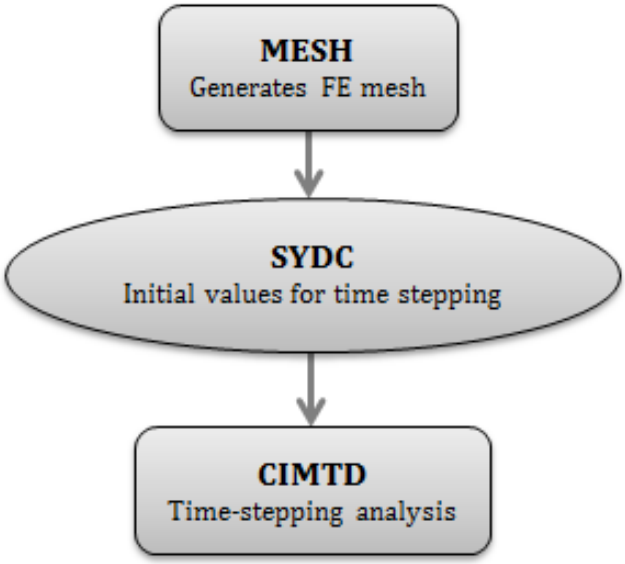

Figure 11: The steps in the FCSMEK simulation.

ecuted by running the program $SYDC$, this requires the initial machine parameters for the time stepping simulation e.g. supply source, connection type, rotation angle of the rotor and temperature of the rotor and stator of the machine. The final step requires running a time stepping simulation based on the initial values given. This is executed using the program $CIMTD$; the inputs are the number of time-steps per one period and the total number of time-step to be simulated.

The results of the simulation initiated by the program $SYDC$ are stored in the file *sydc.tulos*; this contains the machine parameters needed for the stress computation. The results from the time-step simulation were stored in the file *cim.losses*; this contains results from the time-step simulation such as the losses, current density in slots e.t.c. The results obtained from this simulation were used as input parameters in COMSOL Multiphysic for the study of the mechanical stress distribution due to the magnetic forces.

The finite-element analysis of the mechanical stress due to magnetic forces was done in a rotating-mechinery-magnetic physics in COMSOL Multiphysics. The equations which defined the magnetic field computation in the rotating-machinery-magnetic physics in the time-dependent study is given by

$$\bar{\sigma}\frac{\partial \boldsymbol{A}}{\partial t} + \nabla \times \boldsymbol{H} = \boldsymbol{J} \tag{3.17}$$

$$\boldsymbol{B} = \nabla \times \boldsymbol{A} \tag{3.18}$$

$$\nabla \cdot \left(\mu_0 \mu_{\mathrm{r}} \boldsymbol{H}\right) = 0 \tag{3.19}$$

Where $\boldsymbol{A}$ is the vector potential, $\boldsymbol{H}$ is the magnetic field strength, $\boldsymbol{B}$ is the magnetic flux density and $\boldsymbol{J}$ is the current density. $\bar{\sigma}$ is the conductivity of the material, while μ_0 and μ_r are the permeability in free space and the relative permeability of the material respectively.

The computation of the magnetic forces and torque uses an approach which integrates the Maxwell's stress tensor over the exterior surfaces of the set domains. The expression which defined the magnetic force is given by

$$\boldsymbol{F} = d \int_{\partial\Omega} (\boldsymbol{n} \cdot \boldsymbol{\tau}) \, \mathrm{dS} \tag{3.20}$$

where $\boldsymbol{F}$ is the total force, $\boldsymbol{\tau}$ is the stress tensor and $\boldsymbol{n}$ is a normal unit-vector.

The stresses due to the magnetic field are obtained by a weak coupling approach solved by the rotating-machinery-magnetic physics and the solid-mechanics physic. In this approach, the magnetic forces due to the Maxwell stress in the magnetic field analysis were implemented as boundary forces in the solid-mechanics analysis; this gives the mechanical stresses due to the magnetic forces on the rotor and stator core of the machine.

The total stress distribution from the mechanical and magnetic analysis was obtained by super-positioning principle. It should be noted that this study does not investigate the effect of the mechanical stress due to the solid mechanic analysis on the magnetic field computation.

4 Results of Analysis

In this section, the results from the analytical and numerical computation of the mechanical stresses which has been described in the preceding sections are presented: these are given in the order of investigation.

We shall begin this section by interpreting the results of the analytical calculation of the mechanical stress distribution due to shrink fitting, centrifugal forces and the total stress discussed in the previous section. These results shall be compared with that of the numerical solution obtained by finite-element method for the same geometry; this comparison is a means of validating the computational accuracy of the numerical method when used for rotor geometry without any slots.

The analytical solutions of the shaft-rotor shrink fitting was obtained for a shaft and hollow cylindrical geometry with dimension: $a = 0$ mm, $c = 40$ mm, $b = 99.25$ mm and $\delta = 3.267 \cdot 10^{-2}$ mm.

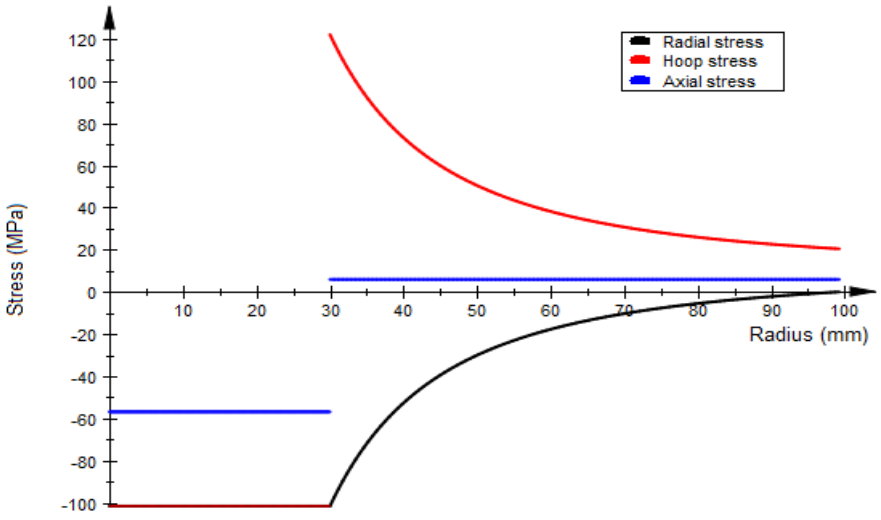

Figure 12: Stress distribution in solid rotor-shaft shrink-fit computed analytically.

The maximum contact pressure obtained from both the analytic and numerical computation is $p_c = 101.6$ MPa. We observed that the analytical method give a very good result when compared to the solution of the numerical computation. It is shown that the *radial*, *hoop* or *circumferential* and *axial* stress in Figure 12 coincides with the simulated results: σ_r, σ_θ and σ_z shown in Figure 13. These results imply that the stresses distributed at the inner cylinder are dominantly compressive, while at the outer cylinder it is tensile.

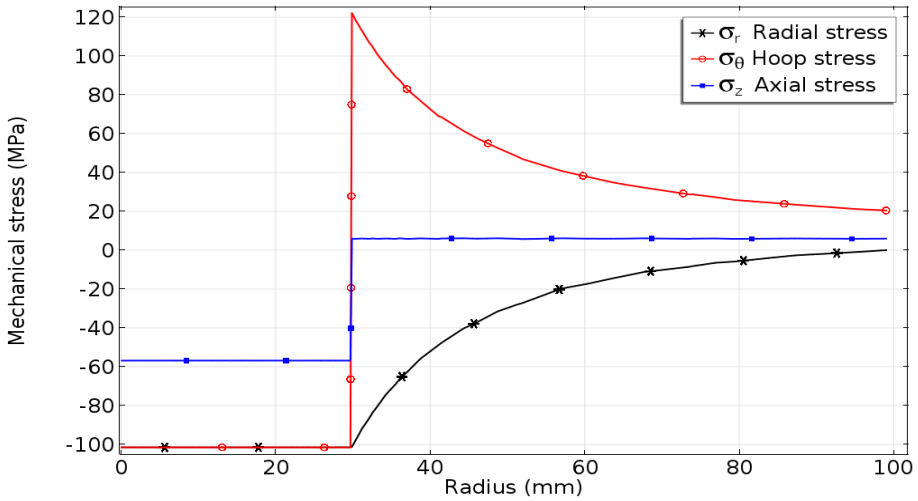

Figure 13: Stress distribution in solid rotor-shaft shrink-fit computed numerically.

Figures of the results from the other analysis presented in Section 3.1 for solid symmetric shaft-rotor fitting and their comparisons with the numerical solutions are shown in Appendix D; the dimensions of the compound geometry are also given. These results gives an idea of how the stress distribution would behave for a more complex shrink fitted geometry: like the synchronous reluctance machine in this study.

4.1 Effect of Shrink Fit

The results of the analytical solution discussed earlier in this section are for geometry without slots. The solutions of the analytical computation for the radial and circumferential stresses are in agreement with the simulated results. The rest of this section focusses on the results of the numerical analysis of the mechanical stresses.

The results obtained from the investigation of the effect of shrink fitting on the rotor and stator of the synchronous reluctance machine described in Section 3.2.2 shall be presented in this section. The mechanical stresses computed are for the maximum radial interference values for the rotor-shaft $\delta_{\text{sr}} = 3.267 \cdot 10^{-2}$ (mm) which gives a maximum contact pressure 75.4 MPa and the sator-frame $\delta_{\text{sf}} = 2.758 \cdot 10^{-1}$ (mm) which gives a contact pressure 13.4 MPa.

The simulated results for the shrink fitted rotor core show that the stresses distribution is not symmetrically distributed at the interface due to the slots (flux barriers) in the rotor geometry. The first principal stresses due to shrink fitting for the maximum values of radial interference obtained for both rotor-shaft and stator-frame fitting are shown in Figures 14 and 15 respectively. The first principal stress distributions are mostly used by engineers to describe the distortion or deformation of material domain due to resultant forces in the domain wall when in equilibrium state; and this distortion is known to cause negative effect on the magnetic proper-

ties of electrical iron core.

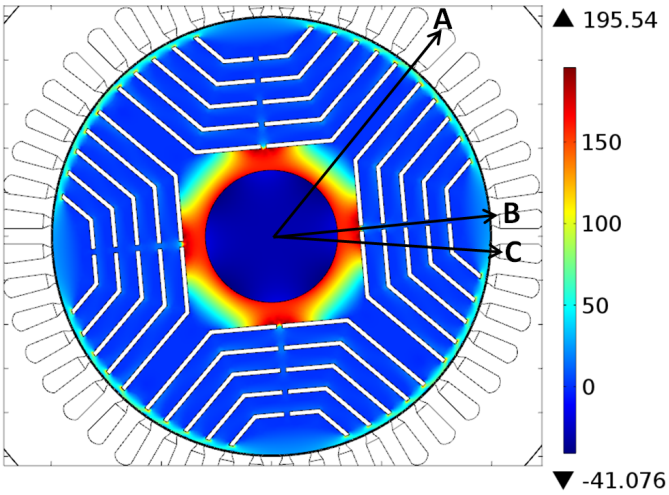

Figure 14: First principal stress due to shrink-fit at rotor core $\delta_{\mathrm{sr}} = 3.267 \cdot 10^{-2}$[mm].

For the purpose of understanding the distribution of the stresses in the complex (synchronous reluctance machine) geometry, the stresses were studied along three paths A, B and C as shown in Figure 14. These stress distributions were investigated for the five different radial interference values given in Table 3.

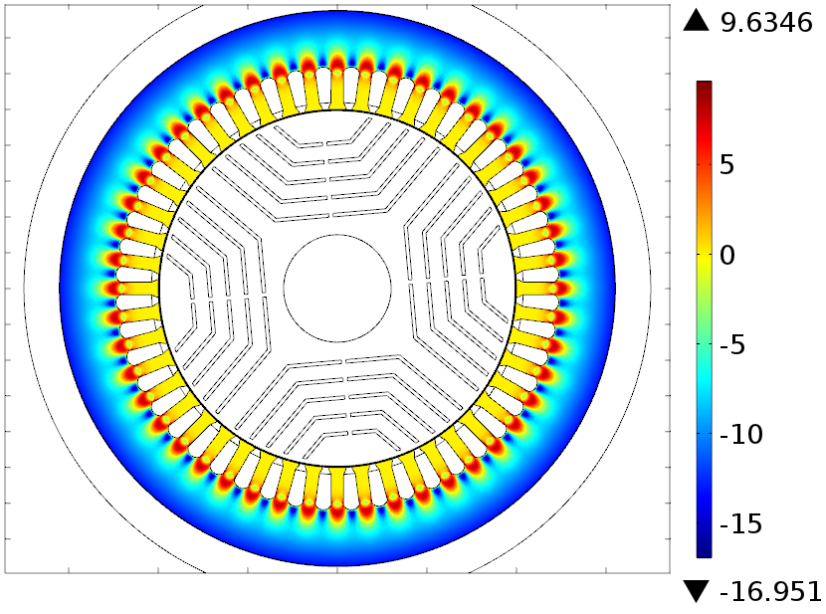

Figure 15: First principal stress due to shrink-fit at stator core $\delta_{\mathrm{sf}} = 2.758 \cdot 10^{-1}$[mm].

The results of these studies along paths A, B & C for the different values of radial

inferences show large differences in the stress distribution along these paths. This difference can be ascribed to be as a result of flux barriers, width of the flux guide and distance between consecutive flux guide and barriers along paths A & B.

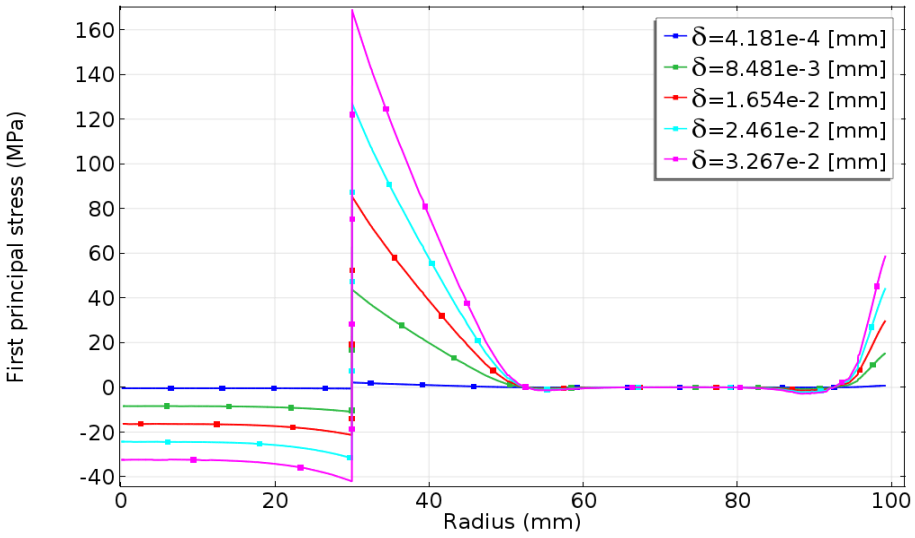

Figure 16: Stress distriburion due to rotor-shaft shrink-fit along path A.

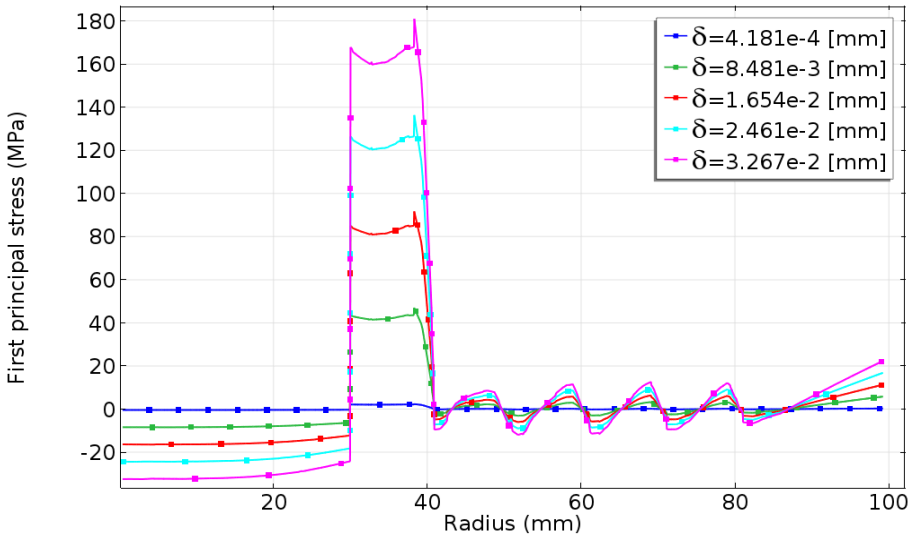

Figure 17: Stress distriburion due to rotor-shaft shrink-fit along path B.

The results obtained show that the stress distribution on the rotor core is mostly tensile and it is very large at positions close to the shrink fitted interfaces, while the shaft is under compressive stress. The stress distribution shows maximum compressive stress and contact pressure along path A. It is also observed that the stress distribution due to shrink fit is almost zero in most parts of the rotor as shown in Figure 16. These stress distributions are due to the axisymmetric nature of the rotor

core due to the presence of slots (flux barriers).

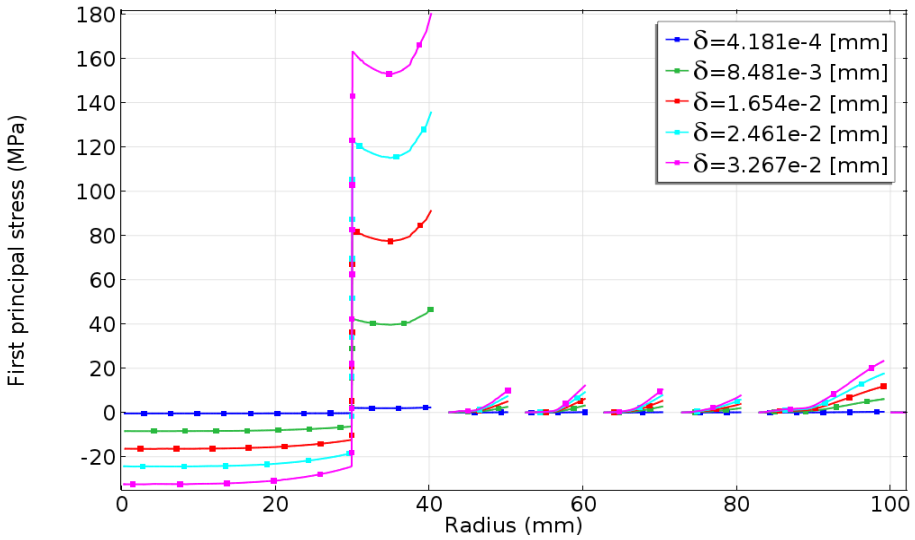

Figure 18: Stress distriburion due to rotor-shaft shrink-fit along path C.

The stress distribution along path B in Figure 17 show a change in the stresses. The compressive stress is reduced and the rotor has maximum tensile stress along this path: these could be due to the length of the laminated core between successive flux barriers. The stress concentration at the edges of the machine path B could also be reduced by increasing the length of the bridge.

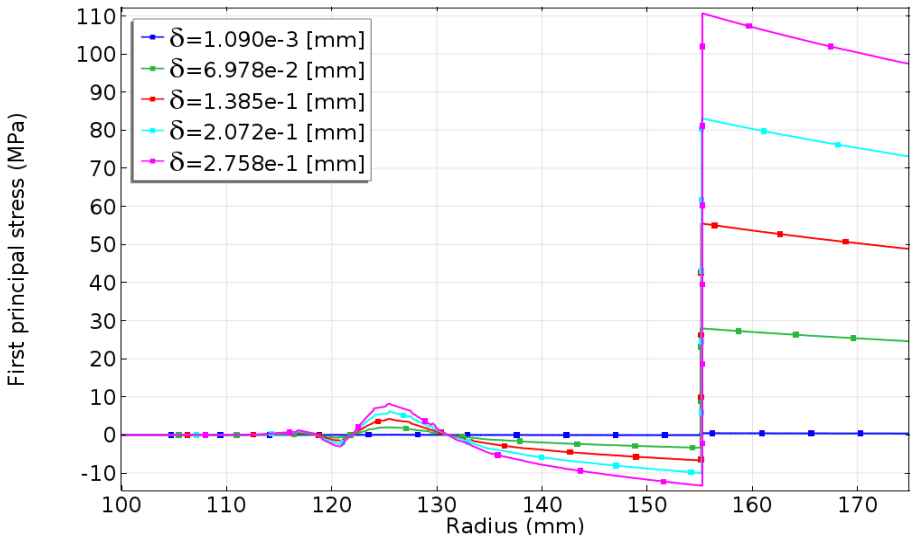

Figure 19: Stress distribution due to stator-frame shrink-fit computed radially across stator teeth.

The stress distribution along path C shows a similar attribute as in Path B at the shaft, while the stresses between flux barriers are drastically reduced. The stresses

can be seen to be dependent on the radial displacement as shown in Figure 16 to 19. Therefore, if the values of the radial interference are increased, the stresses due to shrink fitting also increases, but when reduced the stresses decreases.

On the other hand, at the stator geometry the stresses due to shrink fit are symmetrically distributed. The result shows that most parts of the stator core are under compressive stress, but not at the stator teeth; where the stress is almost zero as shown in Figure 19.

In summary, based on the simulated results obtained, it should be noted that shrink fitting causes very large tensile stress in the rotor core, while at the stator core large compressive stresses are obtained. The largest compressive stress distribution is seen at the shaft which plays no relevance to this investigation. Furthermore, it must be noted that the stresses due to shrink fitting depend on the value of the radial interferences. Therefore, when δ increases, the stress is increased. On the other hand the stress is reduced when δ decreases.

4.2 Centrifugal Force Effect

The results of the numerical computation of the mechanical stresses due to centrifugal force shall be discussed here. The stresses were obtained at the synchronous speed (1500 rpm) for the synchronous reluctance machine operated at a frequency of 50 Hz.

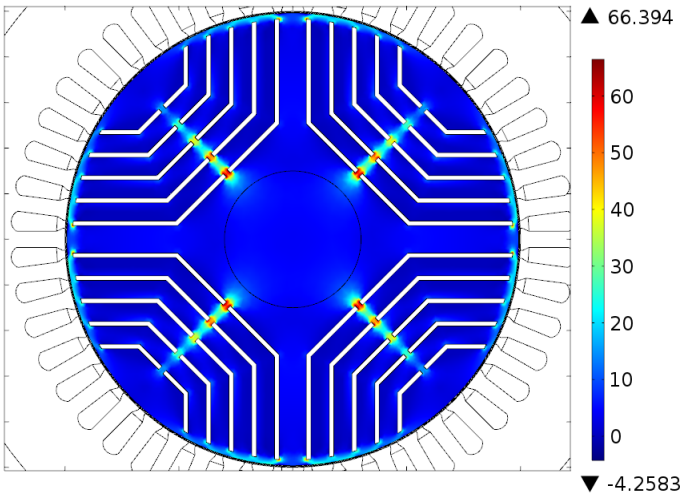

Figure 20: FPS (MPa) distribution due to centrifugal force, f=50 Hz

The mechanical stress distribution obtained by simulation are low and tensile at most parts of the rotor, except at the bridges between successive flux barriers near the interface; where the stresses are large and tensile (up to 66 MPa) for a 50 Hz machine. The study shows large tensile stresses concentration at the edges of slots

and at bridges between flux barriers near the shaft as shown in Figure 20. This analysis shows the effect of the centrifugal forces only for the synchronous reluctance machine.

4.3 Centrifugal Force and Shrink Fit Effect

The results of combination of stresses due to shrink fitting and centrifugal forces on the synchronous reluctance machine are discussed in this section. The results which show the effect of centrifugal forces on the shrink fitted synchronous reluctance machine geometry at a frequency of 50 Hz, 75 Hz and 100 Hz shall be discussed here.

The effect of the centrifugal force at $f = 50$ Hz shows no relevant change in the stress distribution on the rotor geometry in comparison to the effect of shrink fitting only. The stress distribution at this frequency for shrink fitting and centrifugal forces is presented in Figure 21 and Figure 22 respectively. The results of this analysis show that the rated frequency (50 Hz) is obviously a suitable choice in the design of this machine model this is because the maximum stresses along path A & B show no relevant changes.

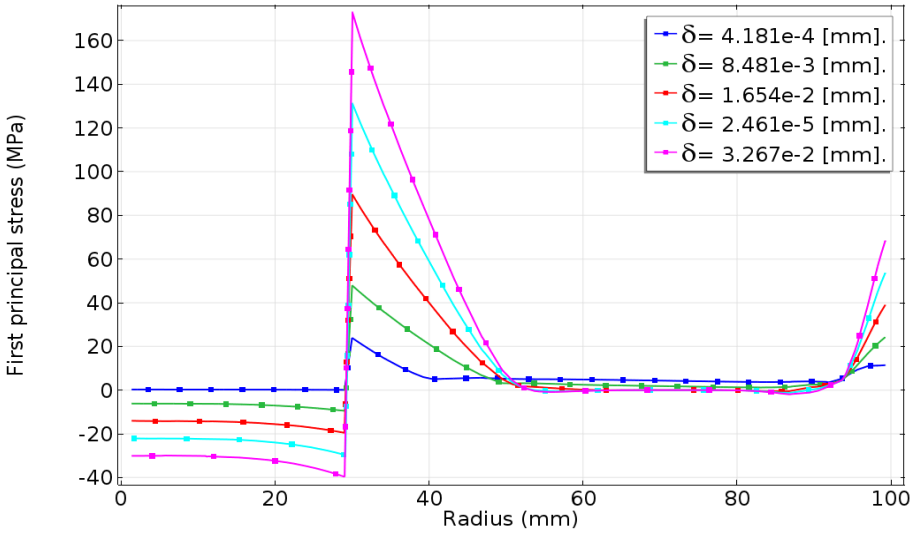

Figure 21: Stresses due to centrifugal force and shrink-fit along direction A at 50 Hz.

The machine was also investigated to study the stress behavior at three different frequencies: 50 Hz, 75 Hz and 100 Hz. The results of the analysis show increase in the tensile stress due to increasing frequency; the increase were observed to be drastic at the edges of slot close to the shrink fit interface. The compressive stress at the shaft also reduces at increasing frequency. At higher frequencies, this could be a problem for this design as the contact pressure along path B & C tend to reduce at the interface; which could cause plastic deformation of the material.

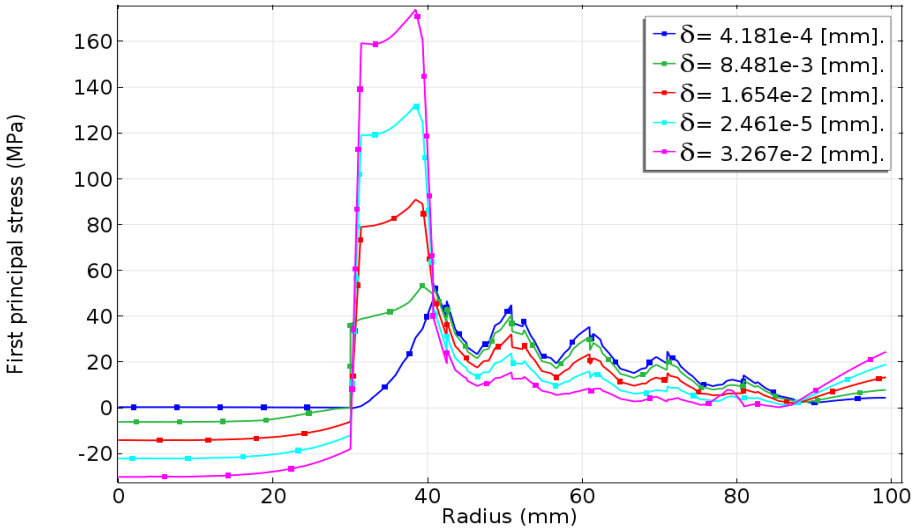

Figure 22: Stresses due to centrifugal force and shrink-fit along direction B at 50 Hz.

From the results of the mechanical stress and shrink fit at 50 Hz frequency, it can be inferred that for an interference displacement of $4.181 \cdot 10^{-4}$ (mm) and $8.481 \cdot 10^{-3}$ (mm), The contact pressure becomes very low. This could cause plastic deformation of the material at the contact interfaces; thereby causing a reduction in the machine life time. To avoid these disadvantages, the machine design should be optimized for the best performance at reduced mechanical stress.

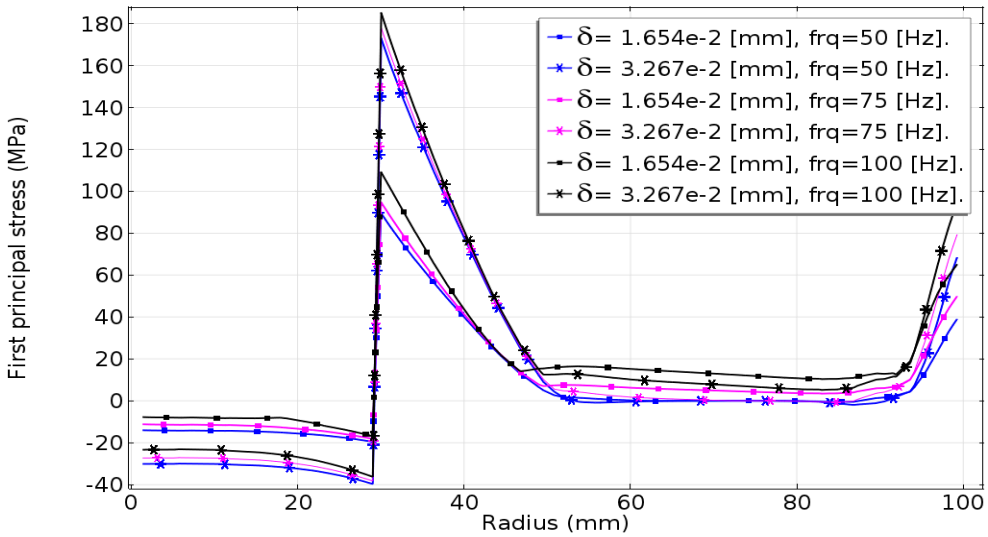

Figure 23: Stresses due to centrifugal force and shrink fit at different frequencies along direction A.

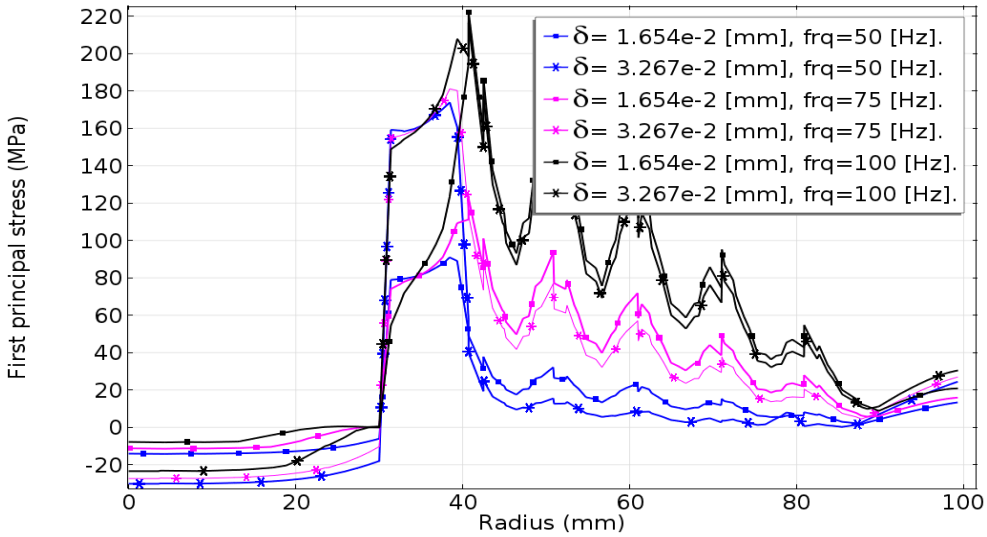

Figure 24: Stresses due to centrifugal force and shrink fit at different frequencies along direction B.

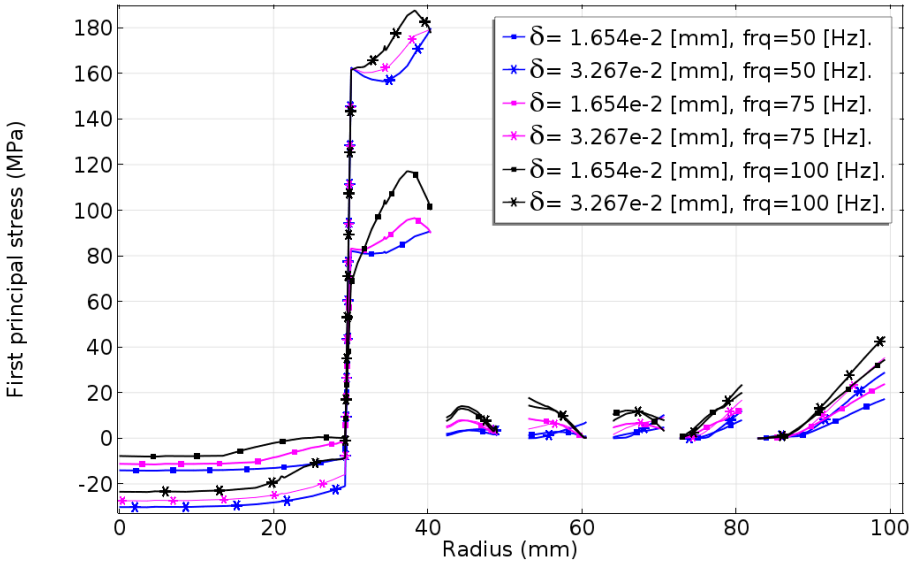

Figure 25: Stresses due to centrifugal force and shrink fit at different frequencies along direction C.

In summary, a numerical analysis has been performed to study the effect of the centrifugal forces on the shrink fitted rotor-shaft geometry. It was found that the tensile stresses at the rotor core increase at increasing frequency. The stress distribution along path B at the bridge between successive flux barriers close to the shrink fitted interface increases drastically at higher frequencies. For this reason, it could be preferable to use a radial interference of $\delta = 3.267 \cdot 10^{-2}$ (mm), if this machine model was intended to be operated at 100 Hz via a control drive system; else, a reduced value of radial interference could be used for a reduced mechanical stress distribution. Simulated results for this along path A, B & C are shown in

Figure 23 to Figure 25.

4.4 Magnetic forces Effect

The results of the mechanical stresses due to the magneto-mechanical effect that have been presented in Section 3.2.3 shall be discussed here. As we have stated earlier, the calculation of the mechanical stresses due to the magnetic forces is a difficult task to achieve by analytical method, as such this analysis was carried out by numerical method.

The principal stress due to the magnetic force on both the rotor and stator core of the rotating machine at rated values are shown in Figure 26. It should be noted that the magnetic forces which yield mechanical stress are dynamic in nature due to the motion of the time-dependent magnetic field.

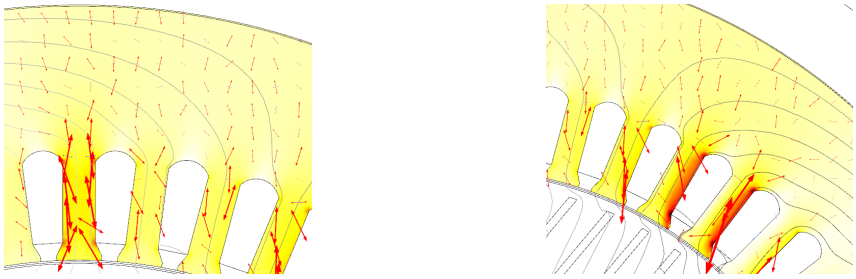

(a) The principle stress surface at (I)

(b) The principle stress surface at (II)

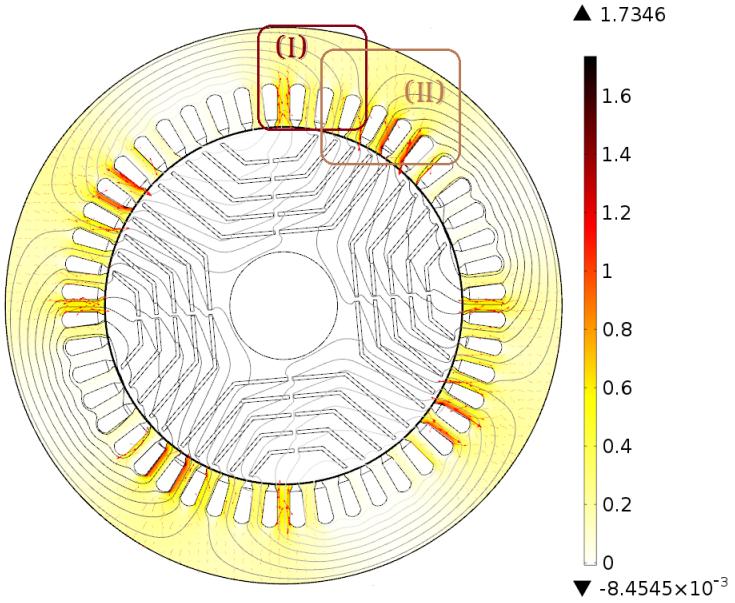

(c) FPS (MPa) and vector potential lines

Figure 26: Mechanical stress distribution due to magnetic forces on stator core.

The stress distributions are proportionally presented by the principal stress surface

(arrow lines); while the z-component of the vector potential line has been used to present the rotating magnetic field as shown in Figure 26. It is shown that the first principal tensile stress (Red-arrow outward) dominates at the stator teeth which imply that the stator teeth are subjected to tensile stresses. At the stator yoke, the first principal tensile stresses and third principal compressive stress (Blue-arrow inward) are sparsely distributed, this shows that the stress distribution due to the magnetic forces at the stator yoke are negligibly small. These are clearly presented in Figure 26a and Figure 26b.

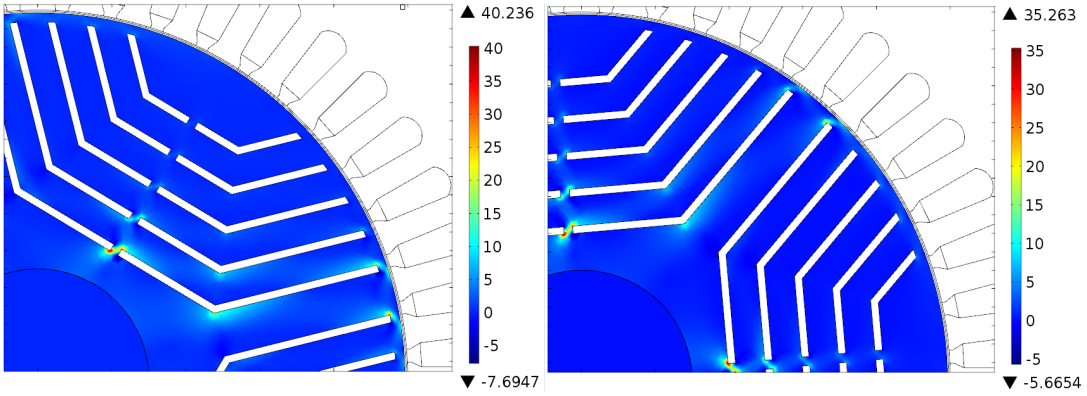

(a) FPS (MPa) due to magnetic forces $t = 36$ ms

(b) FPS (MPa) due to magnetic forces $t = 40$ ms

Figure 27: The FPS (MPa) due to magnetic forces on rotor core

The result of the stress distribution shows quite large stresses at the edges of core materials between successive flux barriers and tensile stress at most parts of the rotor rib. The behaviour of the rotor core at two time instant $t = 40$ ms and $t = 36$ ms are shown in Figure 27. The differences in the stress distribution could be said to be a result of the pulsating effect of the magnetic forces due to the torque ripple.

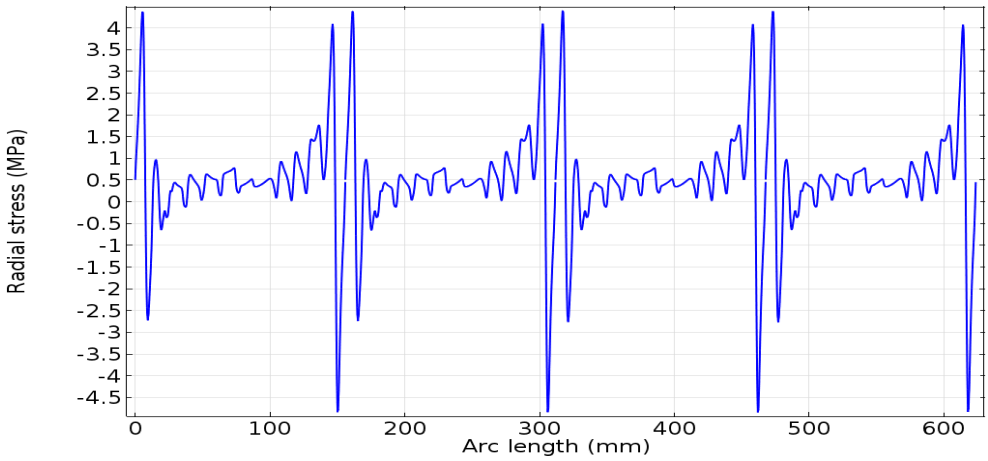

Figure 28: Radial stress (MPa) distribution at rotor surface $t = 40$ ms.

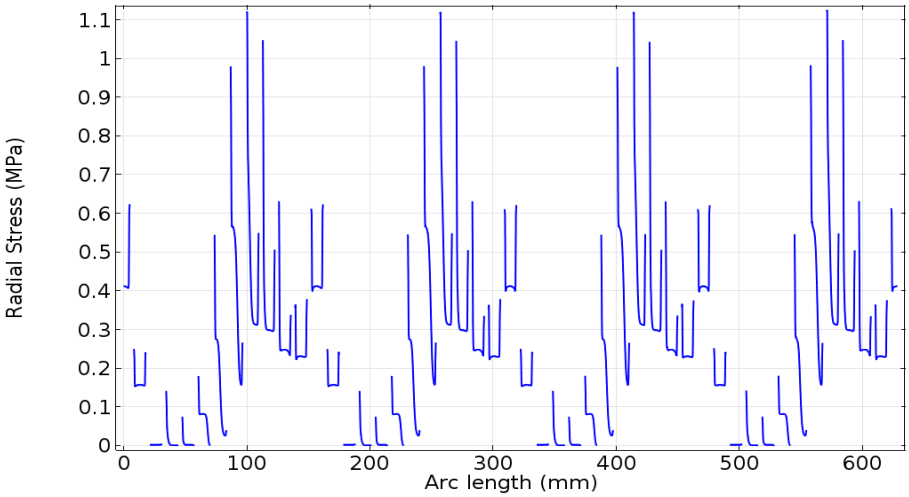

Figure 29: Radial stress (MPa) distribution at stator teeth $t = 40$ ms.

It can be said that though the stresses due to the magnetic forces is low when compared to the effect of shrink fitting and centrifugal forces, the periodic change in the stress distribution could adversely affect on the material properties of the core when the stresses are large. The radial stress distribution at the rotor and stator surface due to the rotating magnetic field are plotted in Figure 28 and Figure 29 for $t = 40$ ms. The radial stresses at the stator teeth are usually tensile and very low.

Combined Stress Effect

The results of the total mechanical stress distribution due to shrink fitting, centrifugal forces and magnetic forces are presented in this section. The stress obtained from the combined stress show that there is radially distributed tensile stress at the stator teeth due to the magnetic force acting radially outward on the stator teeth.

The combined stress distribution shows a unique behavior at the stator core: the maximum stress was located behind the stator slots as depicted in Figure 30. The compressive stress at the yoke can be reduced by decreasing the radial interference in the design.

The stress distribution at the stator teeth due to the combined stress shows similar stress distribution as that due to magnetic forces only as shown in Figure 29. This is because shrink fitting has almost no stress effect at the stator teeth. In addition, cutting issues such as punching are not considered in this study.

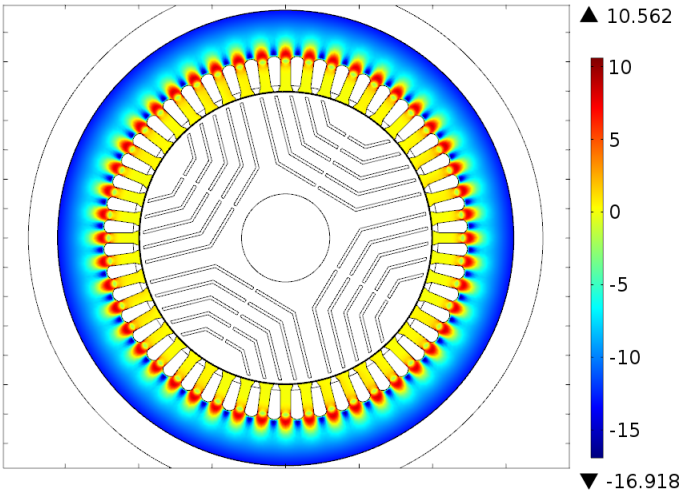

Figure 30: FPS (MPa) due to combined stress effect on stator core $t = 36$ ms.

The effect of the magnetic forces on the rotor core display a unique behavior at different time instants as the stress distribution slightly changes as shown in Figure 31 to Figure 33. This behavior could be attributed to the effect of the pulsating forces due to the torque ripple.

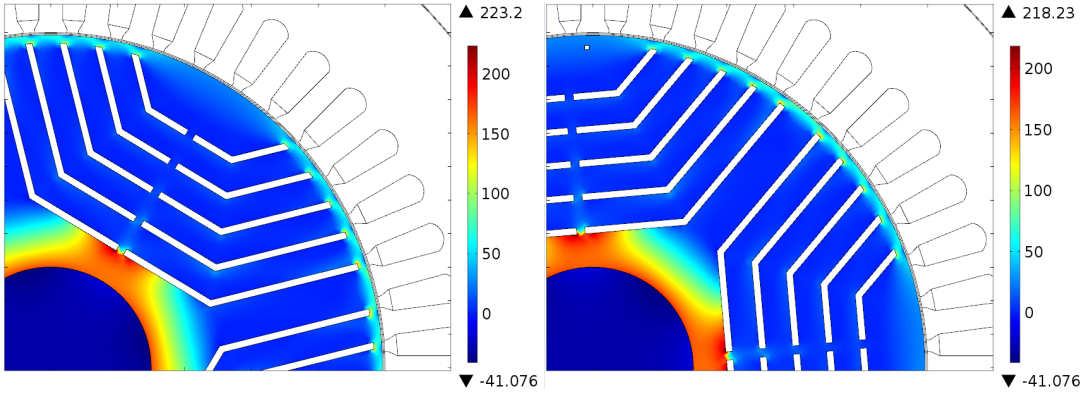

(a) Combined stress effect $t = 36$ ms (b) Combined stress effect $t = 40$ ms

Figure 31: FPS (MPa) due to combined stress effect on rotor core.

The large difference in the radial stress shown in Figure 32 and Figure 33 at different time instants ($t = 36$ ms and $t = 40$ ms) could be due to the numerous flux barriers in the rotor core; which reduces the iron material in the core. As a result, a small force applied at the surface generates large stress at the rotor surface. The width between successive flux barriers should be optimized to obtain a maximum reactance ratio and torque for the machine at a reduced mechanical stress.

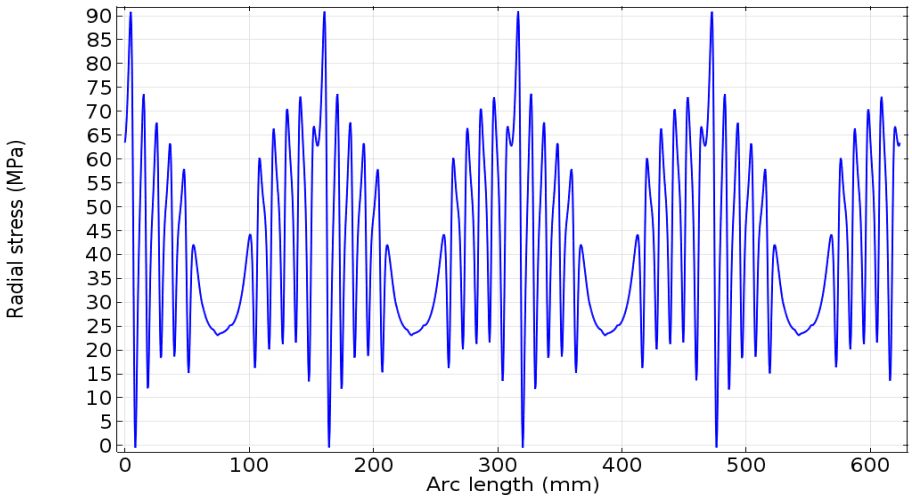

Figure 32: Radial stress (MPa) distribution at rotor outer boundary $t = 36$ ms.

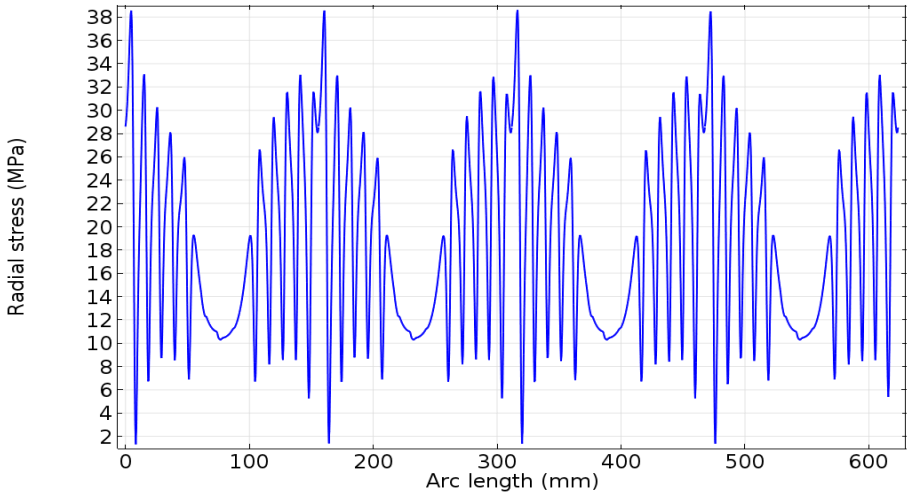

Figure 33: Radial stress (MPa) distribution at rotor outer boundary $t = 40$ ms.

In summary, the total mechanical stresses due to shrink-fitting, centrifugal forces and magnetic forces have been studied. The results of the analysis have shown quite interesting behaviour due to the magneto-mechanical effects at both the rotor and stator core. It has been found that shrink fitting issue has the largest stress effect on the iron core of the synchronous reluctant machine.

To this end, the stress could be minimized by reducing the radial interferences at the rotor and stator interface. The mechanical stress distribution due to the magnetic force is low compared to the shrink fitting and centrifugal forces, but its dynamic nature and how it affects the iron core material over time most especially at large stresses could be detrimental to the machine life. All the stress issues should be considered in the machine optimization in the design of synchronous reluctant machine to minimize losses.

5 Discussion

The mechanical stress distributions due to shrink fitting, centrifugal forces and magnetic forces in a synchronous reluctance machine model have been investigated by finite-element methods. The analysis also included the use of analytical methods in the computation of the radial and circumferential stresses for solid rotor geometry. The results of the analytical model were validated by numerical methods.

The results of the analysis of stresses in the synchronous reluctant machine show that the mechanical stresses are not symmetrically distributed at the interface of the rotor and shaft fitting. The asymmetric behaviour of the stresses at this interface was attributed to occur due to the flux barriers on the rotor geometry; this was not an issue in the solid rotor geometry.

In the synchronous reluctant machine, the maximum contact pressure was obtained along path A (the d-axis direction) and reduced along the q-axis due to the geometrical structure of the rotor core. The mechanical stresses at the rotor core were mostly tensile for the three stress condition and total stress distribution. The maximum tensile stress occurs at the bridge between flux barriers closest to the shrink fitted interface. These stresses could be reduced by increasing the width of the bridges between flux barriers. The shrink-fitting on the other hand causes uniformly distributed compressive stress at the shaft geometry.

The combined effect of the shrink fitting, centrifugal forces and the magnetic forces on the mechanical stresses studied show that the shrink fitting issues have the largest effect on the mechanical stress distribution, these stresses were found to be dependent on the radial interference: that is at large value of radial interference the mechanical stresses are increased, but at reduced radial interferences, the stresses at the rotor and stator geometry are reduced. On the other hand, the magnetic forces have the least effect on the mechanical stress distribution of the synchronous reluctant machine.

The method implemented in this study uses weakly coupled method to calculate the total stress distribution: the magneto-mechanical analysis follow a unidirectional approach. It does not account for the effect of the stresses due to shrink fitting and centrifugal forces on the magnetic properties of the iron core used in the magnetic field analysis, it only implements the effect of the magnetic force from the magnetic field analysis on the geometrical structure used in total mechanical stress computation. In future analysis, the effect of these stresses on magnetic properties could be implemented in the study to obtain better results. Experimental investigation of these processes and how the stresses could affect the magnetic properties and total losses in the synchronous machine could be very interesting and innovative for machine designers.

In conclusion, it is imperative that designer take all the conditions causing mechani-

cal stress issues into consideration in the design optimization of electrical machines. In designs with multiple flux barriers, the operating frequencies should be such that the total stress distribution at the edges of slots does not result in plastic deformation of the machine geometry.

References

Ali, K., Atallah, K. and Howe, D. (1997), 'Prediction of mechanical stress effects on the iron loss in electrical machines', *J. Appl. Phys.* **81**(8), 4119–4121.

Arkkio, A. (1987), Analysis of Induction Motors Based on the Numerical Solution of the Magnetic Field and Circuit Equations, PhD thesis, Helsinki University of Technology.

Bastos, J. and Sadowski, N. (2003), *Electromagnetic Modeling by Finite Element Methods*, Electrical Engineering and Electronic Series, Marcel Dekker.

Belahcen, A. (2004), Magnetoelasticity, Magnetic Forces and Magnetostriction in Electrical Machines, PhD thesis, Helsinki University of Technology.

Belahcen, A. (2005), 'Magnetoelastic coupling in rotating electrical machines', *IEEE Trans. Magn.* **41**(5), 1624–1627.

Belahcen, A. and Arkkio, A. (2006), Local magneto-mechanical coupling in electrical machines, *in* '2006 12th Biennial IEEE Conference on Electromagnetic Field Computation', pp. 389–389.

Bernard, Y. and Ossart, F. (2004), 'Comparison between two models of magnetic hysteresis accounting for stress', *Int. J. Appl. Electrom.* **19**, 551–556.

Bertotti, G. (1988), 'General properties of power losses in soft ferromagnetic materials', *IEEE Trans. Magn.* **24**(1), 621 –630.

Besbes, M., Ren, Z. and Razek, A. (1996), 'Finite element analysis of magneto-mechanical coupled phenomena in magnetostrictive materials', *IEEE Trans. Magn.* **32**(3), 1058–1061.

Bianchi, N. (2005), *Electrical Machine Analysis Using Finite Elements*, Power Electronics And Applications, Crc.

Bickford, W. B. (1998), *Advanced Mechanics of Materials*, Addison-Wesley.

Bozorth, R. (1993), *Ferromagnetism*, IEEE Press Classic Reissue, Wiley.

Carpenter, C. J. (1960), 'Surface-integral methods of calculating forces on magnetized iron parts', *Proceedings of the IEE - Part C: Monographs* **107**(11), 19–28.

Coulomb, J. L. (1983), 'A methodology for the determination of global electromechanical quantities from a finite element analysis and its application to the evaluation of magnetic forces, torques and stiffness', *IEEE Trans. Magn.* **19**(6), 2514–2519.

Coulomb, J. L. and Meunier, G. (1984), 'Finite element implementation of virtual work principle for magnetic or electric force and torque computation', *IEEE Trans. Magn.* **20**(5), 1894–1896.

DIN 7190 (2001), 'Interference fits–calculation and design rules'.

Dupre, L., Bertotti, G. and Melkebeek, J. A. A. (1998), 'Dynamic preisach model and energy dissipation in soft magnetic materials', *IEEE Trans. Magn.* **34**(4), 1168–1170.

Fonteyn, K., Belahcen, A., Kouhia, R., Rasilo, P. and Arkkio, A. (2010a), 'F e m for directly coupled magneto-mechanical phenomena in electrical machines', *IEEE Trans. Magn.* **46**(8), 2923–2926.

Fonteyn, K., Belahcen, A., Rasilo, P., Kouhia, R. and Arkkio, A. (2010b), Simulated results and experimental verification of a novel magneto-mechanical coupled method, *in* 'Electrical Machines and Systems (ICEMS), 2010 International Conference on', pp. 1743–1748.

Foster, K. (1984), 'Stress and induction dependence of hysteresis losses in electrical steels', *J. Appl. Phys.* **55**(6), 2127–2129.

Foster, K. and Littmann, M. F. (1985), 'Factors affecting core losses in oriented electrical steels at moderate inductions (invited)', *J. Appl. Phys.* **57**(8), 4203–4208.

Foster, K., Werner, F. E. and Del Vecchio, R. (1982), 'Loss separation measurements for several electrical steels', *J. Appl. Phys.* **53**(11), 8308–8310.

Fujisaki, K., Hirayama, R., Kawachi, T., Satoh, S., Kaidou, C., Yabumoto, M. and Kubota, T. (2005), Motor core iron loss analysis evaluating shrink fit and stamping effect by finite element method, *in* 'Digests of the IEEE International Magnetics Conference, 2005. INTERMAG Asia 2005.', pp. 1783–1784.

Fujisaki, K., Hirayama, R., Kawachi, T., Satou, S., Kaidou, C., Yabumoto, M. and Kubota, T. (2007), 'Motor core iron loss analysis evaluating shrink fitting and stamping by finite-element method', *IEEE Trans. Magn.* **43**(5), 1950–1954.

Graham, C. D. (1982), 'Physical origin of losses in conducting ferromagnetic materials', *J. Appl. Phys.* **53**(11), 8276–8280.

Gros, L., Reyne, G., Body, C. and Meunier, G. (1998), 'Strong coupling magneto mechanical methods applied to model heavy magnetostrictive actuators', *IEEE Trans. Magn.* **34**(5), 3150–3153.

Hamrock, B., Jacobson, B. and Schmid, S. (1999), *Fundamentals of machine elements*, McGraw-Hill international editions, WCB/McGraw-Hill.

Hearn, E. (1997*a*), *Mechanics of Materials 2: The Mechanics of Elastic and Plastic Deformation of Solids and Structural Materials*, Elsevier Science.

Hearn, E. (1997*b*), *Mechanics of Materials Volume 1: An Introduction to the Mechanics of Elastic and Plastic Deformation of Solids and Structural Materials*, Elsevier Science.

Hirsinger, L. and Billardon, R. (1995), 'Magneto-elastic finite element analysis including magnetic forces and magnetostriction effects', *IEEE Trans. Magn.* **31**(3), 1877–1880.

Kaido, C. (1991), 'Mechanical method of iron loss measurement in a rotational field and analysis of iron loss in a motor', *J. Appl. Phys.* **69**(8), 5106–5108.

Kank, A., Kumbhar, G. and Kulkarni, S. (2006), Coupled magneto-mechanical field computations, *in* 'International Conference on Power Electronics, Drives and Energy Systems, 2006. PEDES '06.', pp. 1–4.

Leonardi, F., Matsuo, T. and Lipo, T. (1996), Iron loss calculation for synchronous reluctance machines, *in* 'Proceedings of the 1996 International Conference on Power Electronics, Drives and Energy Systems for Industrial Growth, 1996.', Vol. 1, pp. 307 –312.

LoBue, M., Basso, V., Fiorillo, F. and Bertotti, G. (1999), 'Effect of tensile and compressive stress on dynamic loop shapes and power losses of fe-si electrical steels', *J. Magn. Magn. Mater.* **196-197**(0), 372 – 374.

Menard, K. (2002), *Dynamic Mechanical Analysis: A Practical Introduction*, Taylor & Francis.

Miyagi, D., Miki, K., Nakano, M. and Takahashi, N. (2010), 'Influence of compressive stress on magnetic properties of laminated electrical steel sheets', *IEEE Trans. Magn.* **46**(2), 318–321.

Moses, A. and Rahmatizadeh, H. (1989), 'Effects of stress on iron loss and flux distribution of an induction motor stator core', *IEEE Trans. Magn.* **25**(5), 4003–4005.

Özel, A., Şemsettin Temiz, Aydin, M. D. and Şen, S. (2005), 'Stress analysis of shrink-fitted joints for various fit forms via finite element method', *Materials & Design* **26**(4), 281 – 289.

Permiakov, V., Dupré, L., Makaveev, D. and Melkebeek, J. (2002), 'Dependence of power losses on tensile stress for fe-si nonoriented steel up to destruction', *J. Appl. Phys.* **91**(10), 7854–7856.

Permiakov, V., Dupré, L., Pulnikov, A. and Melkebeek, J. (2004), 'Loss separation and parameters for hysteresis modelling under compressive and tensile stresses', *J. Magn. Magn. Mater.* **272-276**(0), E553 – E554.

Permiakov, V., Pulnikov, A., Dupré, L., De Wulf, M. and Melkebeek, J. (2003), 'Magnetic properties of fe-si steel depending on compressive and tensile stresses under sinusoidal and distorted excitations', *J. Appl. Phys.* **93**(10), 6689–6691.

Pulnikov, A., Permiakov, V., Wulf, M. D. and Melkebeek, J. (2003), 'Measuring setup for the investigation of the influence of mechanical stresses on magnetic properties of electrical steel', *J. Magn. Magn. Mater.* **254-255**(0), 47–49.

Sen, P. (1997), *Principles of electric machines and power electronics*, John Wiley & Sons.

Steinmetz, C. P. (1892), 'On the law of hysteresis', *Transactions of the American Institute of Electrical Engineers* **IX**(1), 1–64.

Stranges, N. and Findlay, R. (2000), 'Measurement of rotational iron losses in electrical sheet', *IEEE Trans. Magn.* **36**(5), 3457–3459.

Takahashi, N. and Miyagi, D. (2008), Examination of magnetic properties of electrical steels under stress condition, *in* 'The International Conference on Electrical Engineering 2008', pp. 1–5.

Takahashi, N. and Miyagi, D. (2011), Effect of stress on iron loss of motor core, *in* '2011 IEEE International Electric Machines Drives Conference (IEMDC)', pp. 469–474.

Takahashi, N., Morimoto, H., Yunoki, Y. and Miyagi, D. (2008), 'Effect of shrink fitting and cutting on iron loss of permanent magnet motor', *J. Magn. Magn. Mater.* **320**(20), e925–e928.

Yamamoto, K.-i., Sasaki, T. and Yamashiro, Y. (1999), 'Effects of stress changes after demagnetization on magnetization curves and domain wall motions in a grain-oriented si–fe sheet', *J. Appl. Phys.* **85**(8), 6013–6015.

Yamamoto, K.-I., Shimomura, E., Yamada, K. and Sasaki, T. (1998), 'Effects of external stress on magnetic properties in motor cores', *Electrical Engineering in Japan* **123**(1), 15–22.

Yang, Q., Yan, R., Fan, C., Chen, H., Liu, F. and Liu, S. (2006), A magneto-mechanical strong coupled model for giant magnetostrictive force sensor, *in* '2006 12th Biennial IEEE Conference on Electromagnetic Field Computation', pp. 337–337.

Zhang, Y., Cheng, M. and Pillay, P. (2011), 'A novel hysteresis core loss model for magnetic laminations', *IEEE T. Energy Conver.* **26**(4), 993 –999.

Zirka, S., Moroz, Y., Marketos, P. and Moses, A. (2010), 'Loss separation in nonoriented electrical steels', *IEEE Trans. Magn.* **46**(2), 286 –289.

A Values of Constants

Shaft-Rotor Shrink Fit

To solve the expression for the constants in the expression given in equation (3.4a) to (3.5b). First, the conditions defined in Section 3.1.1.1 are considered giving the interface displacements

$$u_{\mathrm{i}} = \mathrm{C}_1 r \tag{A-1}$$

$$u_{\mathrm{o}} = \mathrm{C}_3 r + \frac{\mathrm{C}_4}{r} \tag{A-2}$$

By implementing the boundary conditions on equations for the shaft and rotor we obtain

$$\mathrm{C}_1 = \frac{\frac{\delta}{c}(2\upsilon_{\mathrm{i}} - 1)(\upsilon_{\mathrm{i}} + 1)(b^2 - c^2)}{\frac{E_{\mathrm{i}}}{E_{\mathrm{o}}}\Big[(\upsilon_{\mathrm{o}} + 1)(b^2 - c^2(2\upsilon_{\mathrm{o}} - 1))\Big] - \Big[(b^2 - c^2)(2\upsilon_{\mathrm{i}} - 1)(\upsilon_{\mathrm{i}} + 1))\Big]} \tag{A-3a}$$

$$\mathrm{C}_3 = \frac{\delta c(1 - 2\upsilon_{\mathrm{o}})(\upsilon_{\mathrm{o}} + 1)}{\Big[(\upsilon_{\mathrm{o}} + 1)(b^2 - c^2(2\upsilon_{\mathrm{o}} - 1))\Big] - \frac{E_{\mathrm{o}}}{E_{\mathrm{i}}}\Big[(b^2 - c^2)(2\upsilon_{\mathrm{i}} - 1)(\upsilon_{\mathrm{i}} + 1))\Big]} \tag{A-3b}$$

$$\mathrm{C}_4 = \frac{\delta b^2 c(\upsilon_{\mathrm{o}} + 1)}{\Big[(\upsilon_{\mathrm{o}} + 1)(b^2 - c^2(2\upsilon_{\mathrm{o}} - 1))\Big] - \frac{E_{\mathrm{o}}}{E_{\mathrm{i}}}\Big[(b^2 - c^2)(2\upsilon_{\mathrm{i}} - 1)(\upsilon_{\mathrm{i}} + 1))\Big]} \tag{A-3c}$$

Stator-Frame Shrink Fit

In the case of the stator-frame shrink fit, the displacement is give by

$$u_{\mathrm{i}} = \mathrm{C}_5 r - \frac{\mathrm{C}_6}{r} \tag{A-4}$$

$$u_{\mathrm{o}} = \mathrm{C}_7 r + \frac{\mathrm{C}_8}{r} \tag{A-5}$$

By implementing the boundary conditions on equations for the stator and frame,

the expressions for the constants obtained are

$$C_5 = \frac{\delta c(b^2-c^2)(2\upsilon_i-1)(\upsilon_i+1)}{\Big[(b^2-c^2)(\upsilon_i+1)(a^2-c^2(2\upsilon_i-1))\Big] + \dfrac{E_i}{E_o}\Big[(c^2-a^2)(\upsilon_o+1)(b^2-c^2(2\upsilon_o-1))\Big]} \tag{A-6a}$$

$$C_6 = \frac{\delta a^2 c(c^2-b^2)(\upsilon_i+1)}{\Big[(b^2-c^2)(\upsilon_i+1)(a^2-c^2(2\upsilon_i-1))\Big] + \dfrac{E_i}{E_o}\Big[(c^2-a^2)(\upsilon_o+1)(b^2-c^2(2\upsilon_o-1))\Big]} \tag{A-6b}$$

$$C_7 = \frac{\delta c(a^2-c^2)(2\upsilon_o-1)(\upsilon_o+1)}{\dfrac{E_o}{E_i}\Big[(b^2-c^2)(\upsilon_i+1)(a^2-c^2(2\upsilon_i-1))\Big] + \Big[(c^2-a^2)(\upsilon_o+1)(b^2-c^2(2\upsilon_o-1))\Big]} \tag{A-6c}$$

$$C_8 = \frac{\delta b^2 c(c^2-a^2)(\upsilon_o+1)}{\dfrac{E_o}{E_i}\Big[(b^2-c^2)(\upsilon_i+1)(a^2-c^2(2\upsilon_i-1))\Big] + \Big[(c^2-a^2)(\upsilon_o+1)(b^2-c^2(2\upsilon_o-1))\Big]} \tag{A-6d}$$

Centrifugal Forces

The expression obtained for the constants after implementing the boundary conditions defined in Section 3.1.2 are given below

$$C_9 = -\frac{\omega^2(\upsilon_i+1)(2\upsilon_i-1)\big[\rho_i(c^2(\upsilon_o-1)^2(E_i\chi_1-E_o\chi_2)) - \rho_o(E_i(\upsilon_i-1)^2(\chi_3+\chi_4+\chi_5))\big]}{8E_i(\upsilon_i-1)^2(\upsilon_o-1)^2\big[\Upsilon_1+\Upsilon_2\big]} \tag{A-7a}$$

$$C_{11} = -\frac{\omega^2(2\upsilon_o-1)(\upsilon_o+1)\big[\rho_i E_o\chi_6 + \rho_0(\upsilon_i-1)^2(E_i\chi_7+E_o\chi_8)\big]}{8E_o(\upsilon_i-1)^2(\upsilon_o-1)^2\big[\Upsilon_1+\Upsilon_2\big]} \tag{A-7b}$$

$$C_{12} = -\frac{b^2c^2r^2\omega^2(\upsilon_o+1)\big[\rho_i E_o\chi_9 + \rho_o(\upsilon_i-1)^2(E_i\chi_{10}+E_o\chi_{11})\big]}{8E_o(\upsilon_i-1)^2(\upsilon_o-1)^2\big[\Upsilon_1+\Upsilon_2\big]} \tag{A-7c}$$

And the constants Υ_1, Υ_2 and χ_1 to χ_{11} are given as

$$\Upsilon_1 = E_i r^2(\upsilon_\mathrm{o}+1)(b^2-2c^2\upsilon_\mathrm{o}+c^2)) \tag{A-8a}$$

$$\Upsilon_2 = -E_o c^2(2\upsilon_\mathrm{i}-1)(\upsilon_\mathrm{i}+1)(b^2-r^2) \tag{A-8b}$$

$$\chi_1 = r^2(2\upsilon_\mathrm{i}-3)(\upsilon_\mathrm{i}-1)(\upsilon_\mathrm{o}+1)(b^2-2c^2\upsilon_\mathrm{o}+c^2) \tag{A-8c}$$

$$\chi_2 = c^2(2\upsilon_\mathrm{i}-1)(b^2-r^2) \tag{A-8d}$$

$$\chi_3 = b^4c^2(4\upsilon_\mathrm{o}^4-8\upsilon_\mathrm{o}^3-\upsilon_\mathrm{o}^2+8\upsilon_\mathrm{o}-3)+b^4r^2(-2\upsilon_\mathrm{o}^3+3\upsilon_\mathrm{o}^2+2\upsilon_\mathrm{o}-3) \tag{A-8e}$$

$$\chi_4 = b^2c^4(1-2\upsilon_\mathrm{o})+b^2c^2r^2(2\upsilon_\mathrm{o}^3-3\upsilon_\mathrm{o}^2-2\upsilon_\mathrm{o}+3) \tag{A-8f}$$

$$\chi_5 = c^4r^2(-4\upsilon_\mathrm{o}^4+8\upsilon_\mathrm{o}^3+\upsilon_\mathrm{o}^2-6\upsilon_\mathrm{o}+2) \tag{A-8g}$$

$$\chi_6 = c^4r^2(2\upsilon_\mathrm{i}-1)(\upsilon_\mathrm{o}-1)^2(-2\upsilon_\mathrm{i}^3+3\upsilon_\mathrm{i}^2+2\upsilon_\mathrm{i}-2) \tag{A-8h}$$

$$\chi_7 = b^4r^2(2\upsilon_\mathrm{o}^3-3\upsilon_\mathrm{o}^2-2\upsilon_\mathrm{o}+3)+c^4r^2(1-2\upsilon_\mathrm{o}) \tag{A-8i}$$

$$\chi_8 = -c^2(b^4-c^2r^2)(2\upsilon_\mathrm{i}-1)(2\upsilon_\mathrm{o}-3)(\upsilon_\mathrm{i}+1)(\upsilon_\mathrm{o}-1) \tag{A-8j}$$

$$\chi_9 = -c^2(2\upsilon_\mathrm{i}-1)(\upsilon_\mathrm{o}-1)^2(-2\upsilon_\mathrm{i}^3+3\upsilon_\mathrm{i}^2+2\upsilon_\mathrm{i}-2) \tag{A-8k}$$

$$\chi_{10} = (2\upsilon_\mathrm{o}-1)((-2\upsilon_\mathrm{o}^3+3\upsilon_\mathrm{o}^2+2\upsilon_\mathrm{o}-3)b^2+c^2) \tag{A-8l}$$

$$\chi_{11} = (b^2-c^2)(2\upsilon_\mathrm{i}-1)(2\upsilon_\mathrm{o}-3)(\upsilon_\mathrm{i}+1)(\upsilon_\mathrm{o}-1) \tag{A-8m}$$

B Tables of Material Properties COMSOL Multiphysics

Table B-1: Aluminium 6061 material properties

	Property	Name	Value	Unit	Property group
✓	Relative permeability	mur	1	1	Basic
✓	Electrical conductivity	sigma	2.326e7[S/m]	S/m	Basic
✓	Relative permittivity	epsilonr	1	1	Basic
✓	Density	rho	2730[kg/m^3]	kg/m^3	Basic
✓	Young's modulus	E	68.9e9[Pa]	Pa	Young's modulus and Poisson's ratio
✓	Poisson's ratio	nu	0.33	1	Young's modulus and Poisson's ratio
	Coefficient of thermal expansion	alpha	23.2e-6[1/K]	1/K	Basic
	Heat capacity at constant pressure	Cp	893[J/(kg*K)]	J/(kg*K)	Basic
	Thermal conductivity	k	155[W/(m*K)]	W/(m*K)	Basic

Table B-2: Copper material properties

	Property	Name	Value	Unit	Property group
✓	Relative permeability	mur	1	1	Basic
✓	Relative permittivity	epsilonr	1	1	Basic
	Electrical conductivity	sigma	5.998e7[S/m]	S/m	Basic
	Coefficient of thermal expansion	alpha	17e-6[1/K]	1/K	Basic
	Heat capacity at constant pressure	Cp	385[J/(kg*K)]	J/(kg*K)	Basic
	Density	rho	8700[kg/m^3]	kg/m^3	Basic
	Thermal conductivity	k	400[W/(m*K)]	W/(m*K)	Basic
	Young's modulus	E	110e9[Pa]	Pa	Young's modulus and Poisson's ratio
	Poisson's ratio	nu	0.35	1	Young's modulus and Poisson's ratio
	Reference resistivity	rho0	1.72e-8[ohm*m]	Ω*m	Linearized resistivity

Table B-3: Iron core material properties

	Property	Name	Value	Unit	Property group
✓	Electrical conductivity	sigma	0[S/m]	S/m	Basic
✓	Relative permittivity	epsilonr	1	1	Basic
✓	Density	rho	7870[kg/m^3]	kg/m^3	Basic
✓	Poisson's ratio	nu	0.29	1	Basic
✓	Young's modulus	E	185e9[Pa]	Pa	Basic
✓	normH	normH	sqrt(H1^2+H2^2+H3^2)		BH curve
✓	Magnetic field norm	normH	HB(normB[1/T])[A/m]	A/m	HB curve
	Relative permeability	mur	BH(rmm.normH)	1	Basic
	Magnetic flux density norm	normB	BH(normH[m/A])[T]	T	BH curve
	normB	normB	sqrt(B1^2+B2^2+B3^2)	T	HB curve

Table B-4: Shaft material properties

	Property	Name	Value	Unit	Property group
✓	Electrical conductivity	sigma	4.032e6[S/m]	S/m	Basic
✓	Relative permittivity	epsilonr	1	1	Basic
✓	Density	rho	7850[kg/m^3]	kg/m^3	Basic
✓	Poisson's ratio	nu	0.28	1	Basic
✓	Young's modulus	E	205e9[Pa]	Pa	Basic
✓	normH	normH	sqrt(H1^2+H2^2+H3^2)		BH curve
✓	Magnetic field norm	normH	HB(normB[1/T])[A/m]	A/m	HB curve
	Relative permeability	mur	1	1	Basic
	Magnetic flux density norm	normB	BH(normH[m/A])[T]	T	BH curve
	normB	normB	sqrt(B1^2+B2^2+B3^2)	T	HB curve

C FCSMEK files

(FCSMEK cim.data)

1	Machine type
4	Number of poles
50.	Frequency of the supply voltage
0.249	Effective (airgap) length of the machine
0.246	Length of the stator core
0.246	Length of the rotor core
0.246	Length of the permanent magnets
310.0E-03	Outer diameter of the stator core
200.0E-03	Inner diameter of the stator core
0	Index for the frame
4	Index for the shape of stator slots
48	Number of stator slots
23.90E-03	H1 (Dimensions of the stator slots;
1.00E-03	H11 see the maps of the slots)
0.0	H12
17.50E-03	H13
0.0	H14
0.0	H15
3.50E-03	B11
6.50E-03	B12
8.80E-03	B13
0.0	B14
0.0	B15
198.50E-03	Outer diameter of the rotor core
60.00E-03	Inner diameter of the rotor core
0.50	Moment of inertia of the rotor
52	Index for the shape of rotor poles
0	Index for the shape of damping bars
5	Number of damping bars per pole
0	Number of slots for the field winding
0	Every second pole-shoe is a mirror image? (0=No, 1=Yes)
10.00E-03	H0 (Dimensions of the rotor pole;
2.50E-03	H01 see the maps of the poles)
0.0	H02
0.0	H03
0.0	H04
0.0	H05

6.00E-03	B01
2.00E-03	B02
8.00E-03	B03
2.50E-03	B04
0.0	B05
0.0	H2 (Dimensions of the damping bars;
0.0	H21 see the maps of the bars)
0.0	H22
0.0	H23
0.0	H24
0.0	H25
0.0	B21
0.0	B22
0.0	B23
0.0	B24
0.0	B25
4	Material index for the stator core
0	Material index for the stator slot wedges
4	Material index for the rotor pole shoes
0	Material index for the opening of the damping bars
4	Material index for the rotor ring
1	Material index for the centre of the rotor
11	Material index for the stator coils
0	Material index for the damping bars
3	Number of phases
2	Number of parallel paths in stator winding
12	Number of conductors in a stator slot
1	Number of layers of the stator winding
12	Coil pitch in slot pitches
0.0645	Resistance of a stator phase
0.0972	End-winding reactance of a stator phase at 50 Hz
22.	Temperature associated with the resistance (C)
0.520	Half of the average length of a coil
0.6	Filling factor of a stator slot
80.00E-03	H40 (Parameters of stator end winding)
55.00E-03	H41
50.00E-03	H42
15.00E-03	H43

FCSMEK sydc.tulus

Connection	STAR
E.M.F of the line	400.0 V
Terminal voltage	400.0 V
Terminal current	79.0 A
Power factor	0.5767 Ind.
Rotation angle	-40.0 El.deg.
Rotation speed	1500.0 rpm
Air-gap torque	199.5 Nm
Apparent power	54.7 kVA
Active power	31.6 kW
Reactive power	44.7 kVAR
Shaft power	31.3 kW
Rotor voltage	0.0 V
Rotor current	0.0 A

Parameters of two-axis model

Ldd	Ldq	Lqd	Lqq
0.0254594	0.0099718	0.0099718	0.0113283

Ldf	Ld	Lq	Up
0.0000000	-0.0118465	0.0086629	0.00

Id	Fd	Iq	Fq
28.84	-0.3417	-107.89	-0.9347

Del	Te1	Te2
-68.62	191.5	0.0

D Figures of Analytical Computation

The figures of the analytical computation are presented below for solid shaft-rotor and stator-frame analysis. The computation assumed the rotor and stator geometry are solid (without slots). The material properties are the same as those used in the numerical analysis of the synchronous reluctance machine.

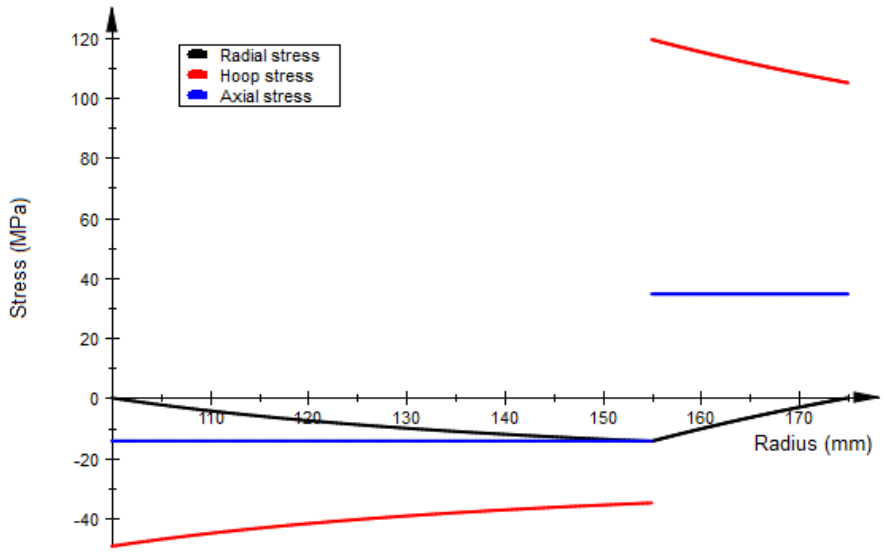

Figure D-1: Stress distribution computed for stator-frame shrink fitting from the equations of Section 3.1.1.2.

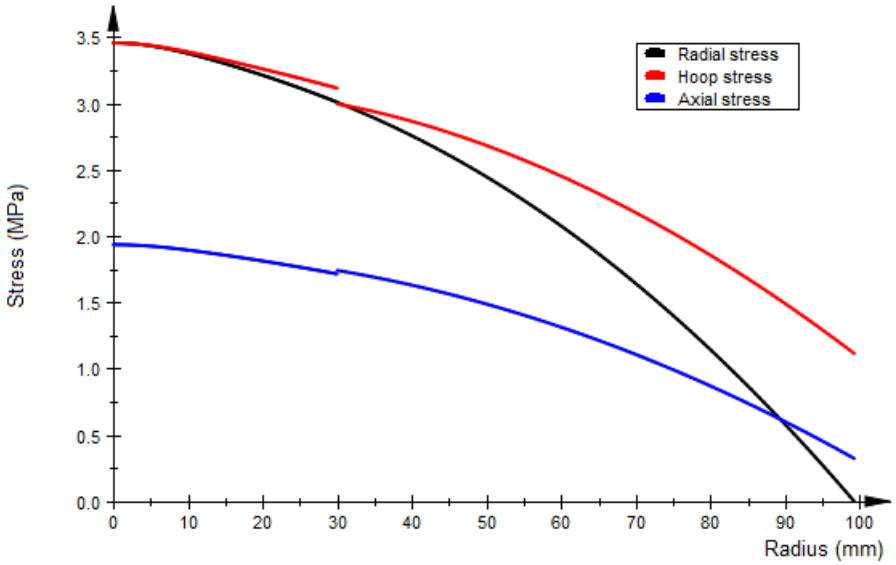

Figure D-2: Stress distribution computed for shaft-rotor due to centrifugal force without shrink-fit from the equations of Section 3.1.2.